Featured in Physics

Spatiotemporal Torquing of Light

S. W. Hancock, S. Zahedpour, A. Goffin, and H. M. Milchberg
Institute for Research in Electronics and Applied Physics, University of Maryland, College Park, Maryland 20742, USA

(Received 3 July 2023; revised 4 January 2024; accepted 10 January 2024; published 28 February 2024)

We demonstrate the controlled spatiotemporal transfer of transverse orbital angular momentum (OAM) to electromagnetic waves: the spatiotemporal torquing of light. This is a radically different situation from OAM transfer to longitudinal, spatially defined OAM light by stationary or slowly varying refractive-index structures such as phase plates or air turbulence. We show that net transverse OAM per photon can be spatiotemporally imparted to a light pulse only if (1) a transient phase perturbation is well overlapped with the pulse in spacetime, or (2) the pulse initially has nonzero transverse OAM density, and the perturbation removes energy from it. Physical insight is provided by the mechanical analogy of torquing a wheel or removing mass as it spins. Our OAM theory for spatiotemporal optical vortex (STOV) pulses [S. W. Hancock *et al.*,Phys. Rev. Lett. **127**, 193901 (2021)] correctly quantifies the light-matter interaction of our experiments and provides a spatiotemporal-torque-based explanation for the first measurement of STOVs [N. Jhajj *et al.*, Phys. Rev. X **6**, 031037 (2016)].

DOI: 10.1103/PhysRevX.14.011031

Subject Areas: Interdisciplinary Physics, Optics, Photonics

I. INTRODUCTION

The study of light carrying longitudinal orbital angular momentum (OAM) has seen a rapid increase in activity since it was realized that Laguerre-Gaussian (LG_{pm}) modes with integer radial and azimuthal indices p and m have an OAM of $m\hbar$ per photon directed parallel or antiparallel to the propagation axis [1]. Whether or not the OAM content was directly important to applications, OAM-carrying light has found uses in areas such as optical trapping [2], superresolution microscopy [3], high-harmonic generation [4], and generation of long air waveguides [5] and plasma waveguides [6]. Other proposed uses of longitudinal OAM beams include free-space communications [7,8], quantum-key distribution [9], and generation of large magnetic fields in intense laser-plasma interaction [10].

That a light pulse could carry an embedded OAM oriented *transverse* to its propagation direction was first revealed in a high-field nonlinear optics experiment [11]. The transverse OAM density was carried by spatiotemporal optical vortices (which we dubbed "STOVs")—vortices embedded in spacetime—generated by the extreme spatiotemporal phase shear produced in the filamentation and self-guiding of intense femtosecond laser pulses in air [11]. STOVs are naturally emergent and necessary electromagnetic structures that govern optical-energy-density flow during self-guided propagation and are a universal consequence of any arrested self-focusing process such as relativistic self-guiding in plasmas [12], all of which involve extreme spatiotemporal phase shear. As they are carried by short pulses and are of finite duration, these structures are necessarily polychromatic [13]. The realization that STOVs were generated by phase shear in spacetime [11] led to a method to generate them linearly and controllably, using a $4f$-pulse shaper device to apply shear in the spatiospectral domain and then return the pulse to the spatiotemporal domain [14–16]. A new single-shot diagnostic, TG-SSSI (transient-grating single-shot supercontinuum spectral interferometry) [17] captured the free-space propagation of pulse-shaper-generated STOV pulses from the near field to the far field with respect to the shaper. Later work used a similar pulse shaper to generate STOVs measured in the far field only [18]. In further work, experiments demonstrating OAM conservation under second-harmonic generation [19–21] verified that transverse OAM is carried by photons. This was an important step because, unlike for a pulse with longitudinal OAM, the spatiotemporal phase winding of a STOV pulse can flip sign or vanish, making it initially less obvious that it carries transverse OAM [22]. Since then, research on STOVs has accelerated, including alternative methods for STOV generation [23–26], investigations of high-harmonic STOV photons from gases and solids [27,28], as well as demonstration of spatiotemporal acoustic vortices [29,30]. We note that STOVs are distinct from stationary,

nonpropagating transverse angular momentum structures, which can be monochromatic [31,32].

Despite the rapidly increasing experimental activity studying STOVs, there had been no theoretical analysis of their OAM content until recently [22,33,34], where our result [22] determined that STOV-based intrinsic OAM must take half-integer values, and the other claiming that only integer values are allowed [33,34]. This difference is more than just an academic question, as it quantifies the exchange of transverse OAM in light-matter interactions. Such interactions, the subject of this paper, are a key building block of future applications of STOVs.

Interactions of longitudinal OAM-carrying beams with matter have long been studied. One early example is the interaction of an LG_{0m} Laguerre-Gaussian donut mode with a macroscopic particle causing it to rotate about the OAM axis [35]. The converse of this process can be viewed as the torquing of light, in which a light beam gains or loses OAM from an interaction with matter. A simple example of this is the pickup of OAM by a beam passing through a spiral phase plate [5] or any refractive-index structure that imparts a nonzero azimuthal phase shift about the propagation axis. For example, LG_{0m} donut beam propagation through a turbulent atmosphere leads to an output beam carrying a spectrum of longitudinal OAM states $m, m \pm 1, m \pm 2, \ldots$ [7,36] owing to the random azimuthal phase shifts picked up over the propagation range. In all of these cases, the OAM beam can be CW and monochromatic, with the refractive-index structures static on the timescale of the beam evolution: Such torquing of light makes preservation of pure longitudinal OAM states difficult.

In this paper, we present the first experimental evidence of the controlled *spatiotemporal* transfer of transverse OAM to light by matter: the spatiotemporal torquing of light. This is a radically different situation from the torquing of longitudinal, spatially defined OAM light by stationary or slowly varying refractive-index structures such as phase plates or air turbulence. We demonstrate that transverse OAM of a light pulse can be changed only for transient phase perturbations well overlapped with the pulse in spacetime, or by removing energy from a pulse already containing nonzero transverse OAM density. We explore the physics of what constitutes an optimal overlap. Furthermore, we experimentally verify our "half-integer" theory of intrinsic STOV OAM [22]; the theory is crucial to correctly quantifying the light-matter interaction of this experiment. We also make a connection with the first measurement of STOVs [11], providing a spatiotemporal-torque-based explanation for their generation.

II. DETERMINING CHANGES IN TRANSVERSE ORBITAL ANGULAR MOMENTUM

The perturbation-induced change in the orbital angular momentum of an optical pulse can be determined from measurements of the amplitude and phase of the pulse before and after the perturbation. For the well-known case of pulses with longitudinal OAM, say, along $\hat{z}$, the procedure is straightforward: If the pre- and postperturbation complex electric fields are E_s and E_{sp}, then the change in longitudinal OAM per photon can be computed as $\Delta\langle L_z\rangle = \langle L_z\rangle_{sp} - \langle L_z\rangle_s = u_{sp}^{-1}\langle E_{sp}|L_z|E_{sp}\rangle - u_s^{-1}\langle E_s|L_z|E_s\rangle$, where $L_z = (\mathbf{r}\times\hat{\mathbf{p}})_z = -i(x\partial/\partial y - y\partial/\partial x)$ is the longitudinal OAM operator, with linear momentum operator $\hat{\mathbf{p}} = -i\nabla$. Here, the expectation values of L_z for the pre- and postperturbation fields are $\langle L_z\rangle_{s,sp} = u_{s,sp}^{-1}\langle E_{s,sp}|L_z|E_{s,sp}\rangle = u_{s,sp}^{-1}\int d^3\mathbf{r} E_{s,sp}^* L_z E_{s,sp}$, with normalizations $u_{s,sp} = \langle E_{s,sp}|E_{s,sp}\rangle = \int d^3\mathbf{r}|E_{s,sp}|^2$, and the integrals taken over all space with $d^3\mathbf{r} = dxdydz$. In order to ensure, in general, that $\Delta\langle L_z\rangle$ is purely intrinsic OAM, the origin must be taken as the energy-density centroid (or "center of energy"). The question of choice of origin in OAM calculations is discussed in Appendix A.1.

The same result for the intrinsic OAM as in the operator-based calculation is obtained by directly integrating the OAM density [1,37] of the fields: $\Delta\langle L_z\rangle = 2k_0U_{sp}^{-1}\int d^3\mathbf{r}[(\mathbf{r}-\mathbf{r}_{sp})\times(\mathbf{E}_{sp}\times\mathbf{H}_{sp}^*)]_z - 2k_0U_s^{-1}\int d^3\mathbf{r}\times[(\mathbf{r}-\mathbf{r}_s)\times(\mathbf{E}_s\times\mathbf{H}_s^*)]_z$, where $\mathbf{r}_{s,sp} = U_{s,sp}^{-1}\int d^3\mathbf{r}\,\mathbf{r}(|\mathbf{E}_{s,sp}|^2 + |\mathbf{H}_{s,sp}|^2)$ are the respective pulse centers of energy, $U_{s,sp} = \int d^3\mathbf{r}(|\mathbf{E}_{s,sp}|^2 + |\mathbf{H}_{s,sp}|^2)$, $\mathbf{H}_{s,sp}$ is the magnetic field, and k_0 is the wave number of the fields, which can be monochromatic. Here we assume propagation in a dilute, nonmagnetic material with index of refraction satisfying $\mathrm{Re}(n) \cong 1$.

Likewise, for changes in intrinsic transverse spatiotemporal OAM, an operator-based calculation should agree with a direct field-based calculation using the transverse OAM density. That is, if E_s and E_{sp} are pre- and postperturbation $\hat{\mathbf{y}}$-polarized pulses propagating along $\hat{\mathbf{z}}$ with transverse OAM oriented along $\hat{\mathbf{y}}$ (ensuring no effects of spin angular momentum), the change in intrinsic transverse OAM per photon $\Delta\langle L_y\rangle$ should be calculable either as

$$\begin{aligned}\Delta\langle L_y\rangle &= \langle L_y\rangle_{sp} - \langle L_y\rangle_s \\ &= u_{sp}^{-1}\langle E_{sp}|L_y|E_{sp}\rangle - u_s^{-1}\langle E_s|L_y|E_s\rangle \end{aligned} \tag{1a}$$

$$\begin{aligned}\text{or } \Delta\langle L_y\rangle = {} & 2k_0'U_{sp}^{-1}\int d^3\mathbf{r}'[(\mathbf{r}'-\mathbf{r}_{sp}')\times(\mathbf{E}_{sp}\times\mathbf{H}_{sp}^*)]_y \\ & - 2k_0U_s^{-1}\int d^3\mathbf{r}'[(\mathbf{r}'-\mathbf{r}_s')\times(\mathbf{E}_s\times\mathbf{H}_s^*)]_y, \end{aligned} \tag{1b}$$

provided that the correct L_y operator is used in Eq. (1a) and the origin is the spacetime center of energy. In Eq. (1b), $\mathbf{r}'$ refers to spacetime coordinates of the pulse (see below) $u_{s,sp} = \int d^3\mathbf{r}'|\mathbf{E}_{s,sp}|^2$, $U_{s,sp} = \int d^3\mathbf{r}'(|\mathbf{E}_{s,sp}|^2 + |\mathbf{H}_{s,sp}|^2)$, and $\mathbf{r}_{s,sp}' = U_{s,sp}^{-1}\int d^3\mathbf{r}'\mathbf{r}'(|\mathbf{E}_{s,sp}|^2 + |\mathbf{H}_{s,sp}|^2)$ are the spacetime centers of energy. Because STOV pulses are polychromatic [22], here k_0 is the central wave number, and k_0' accommodates a central wave-number shift in a spatiotemporally perturbed pulse. For weak perturbations

$k_0' = k_0$, and for negligible absorption or backscattering (see Sec. III) $U_{sp} = U_s$ (and $u_{sp} = u_s$). Our experimental perturbations satisfy both these conditions. The expressions in Eq. (1) also assume nonmagnetic material and $\mathrm{Re}(n) \cong 1$, the conditions of our experiments.

As indicated, care must be taken in determining the form of the spatiotemporal OAM operator L_y. Unlike longitudinal OAM L_z, whose physical origin is the circulation of electromagnetic energy density around the z axis in both x and y dimensions, energy-density flow in a $\hat{\mathbf{z}}$-propagating STOV pulse in vacuum, with OAM along $\hat{\mathbf{y}}$, can occur only along $\pm x$: If any vortex-associated flow occurred along z, it would be superluminal or subluminal above or below the vortex singularity (depending on the sign of the STOV), violating special relativity. In recent work [22], we found a transverse spatiotemporal OAM operator expressed in spacetime rectangular coordinates,

$$L_y = (\mathbf{r}' \times \hat{\mathbf{p}}_{ST})_y = -i\left(\xi \frac{\partial}{\partial x} + \beta_2 x \frac{\partial}{\partial \xi}\right), \qquad (2)$$

which applies in a dispersive optical material. Here, $\xi = v_g t - z$ is a space coordinate relative to the peak of the pulse moving at group velocity v_g, t and z are time and propagation distance in the lab frame, $\beta_2 = v_g^2 k_0 k_0''$ is the dimensionless group velocity dispersion of the material, $k_0'' = (\partial v_g^{-1}/\partial\omega)_{k_0}$, and $\hat{\mathbf{p}}_{ST} = -i\nabla_{ST} = -i(\nabla_\perp - \hat{\boldsymbol{\xi}}\beta_2 \partial/\partial\xi)$ is the spatiotemporal linear momentum operator [22]. For later use in this paper, a lab-frame time interval relative to the pulse center is defined as $\tau = \xi/v_g = t - z/v_g$. In performing the integrals in Eqs. (1a) and (1b), $d^3\mathbf{r}' = dydxd\xi$ in spacetime rectangular coordinates. Here we use rectangular coordinates because our measured complex fields are recorded as rectangular data arrays (see Sec. IV).

Our L_y operator is consistent with special relativity, it conserves electromagnetic energy-density flux, and it is conserved with propagation: $d/dz\langle L_y\rangle = i(2k_0)^{-1}\langle[H, L_y]\rangle = 0$ [22]. Here, $[H, L_y]$ $(= 0)$ is the commutator of L_y and the propagation operator $H = -\nabla_\perp^2 + \beta_2 \partial^2/\partial\xi^2$ from the spacetime paraxial wave equation $2ik_0\partial\mathbf{A}(\mathbf{r}_\perp, \xi; z)/\partial z = H\mathbf{A}(\mathbf{r}_\perp, \xi; z)$ for the field $\mathbf{A}$. In $(\mathbf{r}_\perp, \xi; z)$ coordinates, z plays the role of a timelike running parameter; this is noted by its separation by a semicolon [22]. The transverse OAM operator L_y is also conserved under nonparaxial propagation (see Appendix A.2). It is important to emphasize here that the expectation value $\langle L_y\rangle$ is conserved with propagation irrespective of the origin chosen for its evaluation. For a general choice of origin, $\langle L_y\rangle$ is a sum of intrinsic and extrinsic OAM contributions. Only when the origin is chosen to be the center of energy does the extrinsic contribution vanish, leaving $\langle L_y\rangle$ as the purely intrinsic OAM carried by photons (see Appendix A.1). Recently, another theory for intrinsic transverse OAM has been presented [33,34]; Appendix A.3 compares that approach to our theory [22] and the experiments of this paper.

To illustrate how STOVs propagate and to provide definitions for parameters used later in this paper, Fig. 1(a) reproduces results from Ref. [22], where a STOV pulse of topological charge $l = 1$ and spacetime asymmetry ratio $\alpha = w_{0\xi}/w_{0x} = 0.24$ propagates right to left in air from $z/z_{0x} = -0.41$ to $z/z_{0x} = 0.24$, and right to left within each panel. Here, $w_{0\xi}$ and w_{0x} are timelike and spacelike Gaussian spatial scales of the pulse, and $z_{0x} = k_0 w_{0x}^2/2$ is the spacelike Rayleigh range. The top two rows are spatiotemporal intensity and phase profiles from the analytic modal STOV theory of Ref. [22], and the bottom rows are the corresponding experimental intensity and

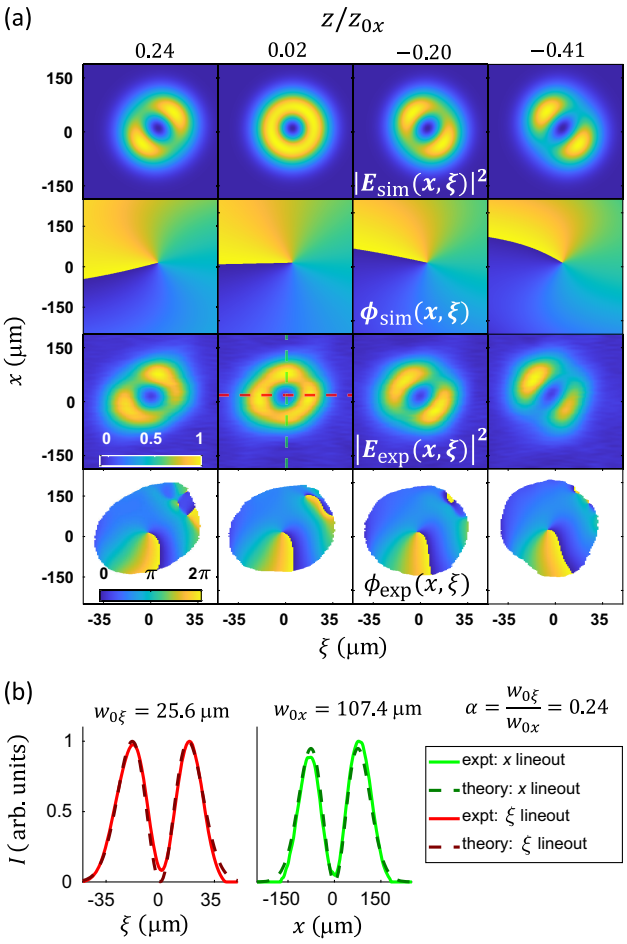

FIG. 1. Illustrative figure of STOV pulse propagation for spacetime asymmetry ratio $\alpha = w_{0\xi}/w_{0x} = 0.24$, with $z_{0x} = \frac{1}{2}k_0 w_{0x}^2 = 4.5$ cm (a) Top two rows: modal theory [22] plots of spatiotemporal intensity and phase of $l = 1$ STOV pulse propagating right to left through its beam waist from $z/z_{0x} = -0.41$ to $z/z_{0x} = 0.24$ (and right to left within each panel). Bottom two rows: experimental intensity and phase plots extracted by TG-SSSI. (b) Lineouts along $(0, \xi)$ and $(x, 0)$ of the experimental intensity profile at $z/z_{0x} = 0.02$ (solid lines) and fits to the modal theory curves (dashed lines).

phase profiles $|E_s(x,\xi)|^2$ and $\phi_s(x,\xi) = \arg[E_s(x,\xi)]$ captured by TG-SSSI [17], where the Gaussian y dependence of the field is not displayed, as it remains unaffected in our experiments and computations. For the room air of the experiments of Ref. [22], as well as in the experiments of this paper, $\beta_2 \cong 1.5 \times 10^{-5}$. This small dispersion has a negligible effect over short air-propagation distances, so for all analyses in Ref. [22] and here, $\beta_2 = 0$ and the transverse OAM operator is $L_y = -i\xi\partial/\partial x$. Note that without the gradient in ξ enabled by nonzero β_2, this operator cannot transport energy density along $\pm\xi$; it is transported only along $\pm x$. As seen in Fig. 1(a), spatial diffraction along $\pm x$ causes the donut shape near $z = 0$ to evolve to lobed structures with opposite spacetime tilt on either side of $z = 0$, while the transverse OAM is conserved throughout propagation.

For a STOV pulse of topological charge l and spacetime asymmetry ratio α propagating in a dispersive medium characterized by β_2, Ref. [22] shows that the expectation value of transverse OAM is $\langle L_y\rangle = \frac{1}{2}l(\alpha - \beta_2/\alpha)$, so that for the air-propagating STOV pulse in Fig. 1, $\langle L_y\rangle = \frac{1}{2}l\alpha = 0.12$. The factor of $1/2$ for the spacetime vortex is a direct result of energy-density circulation restricted to $\pm x$.

III. SPATIOTEMPORAL TORQUE

The goals of our experiments are to (1) explore how spatiotemporal perturbations to electromagnetic fields affect transverse OAM, and (2) verify the correctness of our theoretical approach [22]. For these purposes, it is first useful to introduce the notion of spatiotemporal torque.

For an initial pulse $A_s(x,\xi) = |A_s(x,\xi)|e^{i\phi_s(x,\xi)}$ and a spatiotemporal perturbation $\Gamma(x,\xi) = |\Gamma(x,\xi)|e^{i\Delta\phi_p(x,\xi)}$, where $\phi_s(x,\xi)$ and $\Delta\phi_p(x,\xi)$ are real functions, the perturbed pulse is $A_{sp}(x,\xi) = \Gamma(x,\xi)A_s(x,\xi)$. This formulation assumes that the perturbation does not backscatter light into the pulse; this condition is well satisfied by sufficiently weak perturbations, including those of our experiments, and by perturbations that effectively remove energy from the pulse. We take A_s and A_{sp} to be polarized along $\hat{\mathbf{y}}$ so there are no effects of spin angular momentum. The change of transverse OAM per photon from the perturbation is then (see Appendix A.4)

$$\begin{aligned}\Delta\langle L_y\rangle &= \langle L_y\rangle_{sp} - \langle L_y\rangle_s \\ &= iu_{sp}^{-1}\int dx\,d\xi\left[|A_s|^2|\Gamma|^2 L_y\Delta\phi_p \right. \\ &\quad \left. + |A_s|^2\left(|\Gamma|^2 - \frac{u_{sp}}{u_s}\right)L_y\phi_s\right], \end{aligned} \tag{3}$$

where $u_{sp} = \int dx\,d\xi A_s(x,\xi)|^2|\Gamma(x,\xi)|^2$.

Equation (3) is intuitively appealing. The first term in the integral suggests the notion of "spatiotemporal torque," where the change in OAM is given by an effective force-lever arm product $iL_y\Delta\phi_p = \xi\partial\Delta\phi_p/\partial x + \beta_2 x\partial\Delta\phi_p/\partial\xi$ weighted by the energy-density distribution $|A_{sp}(x,\xi)|^2 = |\Gamma(x,\xi)A_s(x,\xi)|^2$ of the torqued object. Here the "force" components are $\partial\Delta\phi_p/\partial x$ and $\beta_2\partial\Delta\phi_p/\partial\xi$, and the lever arm components are ξ and x. A mechanical analogy for the integral's second term is the change in OAM caused by location-specific mass removal from a spinning wheel. For cases where energy is removed from the pulse by absorption or scattering, $u_{sp}/u_s < 1$, and the second term contributes to the change in OAM provided that the initial pulse has nonzero transverse OAM density $M_y(x,\xi) = A_s^* L_y A_s = i|A_s|^2 L_y\phi_s$; otherwise, $L_y\phi_s = 0$ and the second term vanishes. Effectively, the wheel must already be "spinning" for mass removal to change OAM. Note that the second term will vanish, irrespective of ϕ_s, in the case of a pure phase perturbation where $|\Gamma| = 1$ and $u_{sp}/u_s = 1$. This type of perturbation corresponds to our experiments.

Further examination of Eq. (3) leads to several insights: (a) Pure amplitude perturbations (with $\Delta\phi_p = 0$) that conserve pulse energy cannot change the transverse OAM per photon of a light pulse; in that case, $\Gamma(x,\xi)$ can be viewed as a scattering coefficient that redistributes pulse energy over $\pm x$. (b) Steady-state ($\partial\Delta\phi_p/\partial\xi = 0$) or spatially uniform ($\partial\Delta\phi_p/\partial x = 0$) phase perturbations do not change transverse OAM. (c) The only ways to change transverse OAM per photon are (i) for either or both of the effective force terms $\partial\Delta\phi_p(x,\xi)/\partial x$ and $\beta_2\partial\Delta\phi_p(x,\xi)/\partial\xi$ to be time varying and have an asymmetric temporal overlap with the energy-density distribution (across the pulse's temporal center of energy) or (ii) for energy to be removed from selected spatiotemporal locations in a pulse containing transverse OAM density. In all cases, the spatiotemporal location of the perturbation determines the change in transverse OAM per photon. In atmospheric density gases, β_2 is negligible and $\partial\Delta\phi_p(x,\xi)/\partial x$ is the dominant contribution to the first term of Eq. (3).

To provide physical insight in advance of discussing the experiment, we consider a simple step-function perturbation model. The model corresponds well to our experiments (see Sec. IV) and also provides significant interpretative insight for the first experiment to measure STOVs [11] (see Appendix A.5). We apply the spacetime perturbation $\Gamma(x,\xi) = |\Gamma(x,\xi)|e^{i\Delta\phi_p(x,\xi)}$, with $|\Gamma(x,\xi)| = 1$ and

$$\begin{aligned}\Delta\phi_p(x,\xi) &= \Delta\phi_{p0}[\Theta(x - x_0 + h) - \Theta(x - x_0 - h)] \\ &\quad \times \Theta(\xi - \xi_0)\end{aligned} \tag{4}$$

to either a Gaussian pulse $A_G(x,\xi)$, or to a $l = 1$ STOV pulse $A_{STOV}(x,\xi)$:

$$A_G(x,\xi) = A_0\exp(-x^2/w_{0x}^2 - \xi^2/w_{0\xi}^2), \tag{5a}$$

$$A_{STOV}(x,\xi) = (\xi/w_{0\xi} + ix/w_{0x})A_G(x,\xi). \tag{5b}$$

Here, $\Theta(q)$ is the Heaviside function, $2h$ is the spatial width of the perturbation centered at $x = x_0$, and the perturbation turns on at $\xi = \xi_0$ (or $\tau = \tau_0$). The choice of a phase-only perturbation ($|\Gamma(x,\xi)| = 1$) corresponds to our experimental perturbation (see Sec. IV). The spacelike and timelike widths of the Gaussian pulse are w_{0x} and $w_{0\xi}$, and the expressions for A_{G} and for A_{STOV} are accurate for $z \ll z_{0x} = k_0 w_{ox}^2/2$ [22]. Because transverse OAM is conserved with z, it is sufficient to use these expressions [Eq. (5)] in our calculations. Using Eq. (1a) with initial fields A_{G} or A_{STOV}, the simple perturbation model produces analytic solutions for $\Delta\langle L_y\rangle_{\mathrm{G}}$ and $\Delta\langle L_y\rangle_{\mathrm{STOV}}$ as a function of (x_0, ξ_0):

$$\Delta\langle L_y\rangle_{\mathrm{G}} = \frac{\Delta\phi_{p0}}{2\pi}\left(\alpha + \frac{\beta_2}{\alpha}\right)\left[\exp\left(\frac{8hx_0}{w_{0x}^2}\right) - 1\right]\exp\left(-\frac{2(h+x_0)^2}{w_{0x}^2} - \frac{2\xi_0^2}{w_{0\xi}^2}\right), \tag{6a}$$

$$\begin{aligned}\Delta\langle L_y\rangle_{\mathrm{STOV}} = {} & \frac{\Delta\phi_{p0}}{2\pi}\left(\alpha + \frac{\beta_2}{\alpha}\right)\exp\left(-\frac{2(h+x_0)^2}{w_{0x}^2} - \frac{2\xi_0^2}{w_{0\xi}^2}\right) \\ & \times\left\{\left[\exp\left(\frac{8hx_0}{w_{0x}^2}\right) - 1\right]\left(1 + 2\frac{h^2 + x_0^2}{w_{0x}^2} + 2\frac{\xi_0^2}{w_{0\xi}^2}\right) - \frac{4hx_0}{w_{0x}^2}\left[\exp\left(\frac{8hx_0}{w_{0x}^2}\right) + 1\right]\right\}.\end{aligned} \tag{6b}$$

Figures 2(a) and 2(b) plot $\Delta\langle L_y\rangle_{\mathrm{G}}$ and $\Delta\langle L_y\rangle_{\mathrm{STOV}}$ vs (x_0, ξ_0). Each panel is for a particular half-width h/w_{ox} and normalized dispersion β_2, where $\beta_2 = \pm 1$ is for dense, positively, or negatively dispersive media, and $\beta_2 = 0$ corresponds to low-density media such as air, the propagation medium of our experiment. Plots using the dispersion of air $\beta_2 \cong 1.5 \times 10^{-5}$ are indistinguishable from those using $\beta_2 = 0$.

We first discuss the $\beta_2 = 0$ plots (the plots for the $\beta_2 = 1$ cases are qualitatively similar). Figure 2(a) shows the transfer of transverse OAM to A_{G}, a pulse with zero initial OAM. Maximum OAM transfer occurs for x_0 located at the spatial edges of the pulse ($x_0 \sim \pm w_{0x}$) and for ξ_0 located near the pulse center ($\xi_0 \sim 0$). As discussed earlier in the context of Eq. (3), these optimum zones of (x_0, ξ_0) maximize the overlap of the force-lever arm product with the torqued pulse energy density. Importantly, the perturbation transient [here, the step $\Theta(\xi - \xi_0)$] must overlap with the pulse so that the torque contributions are imbalanced across the temporal center of energy at $\xi = 0$. For $\Theta(\xi - \xi_0)$ located outside the region of the pulse (for $|\xi_0/w_{0\xi}| > \sim 1$), $\Delta\langle L_y\rangle \to 0$ because the pulse sees the perturbation as steady state. The effect on $\Delta\langle L_y\rangle$ of a time- and space- localized spatiotemporal torque is described in Appendix A.6, supporting the analogy of mechanical torque on a wheel.

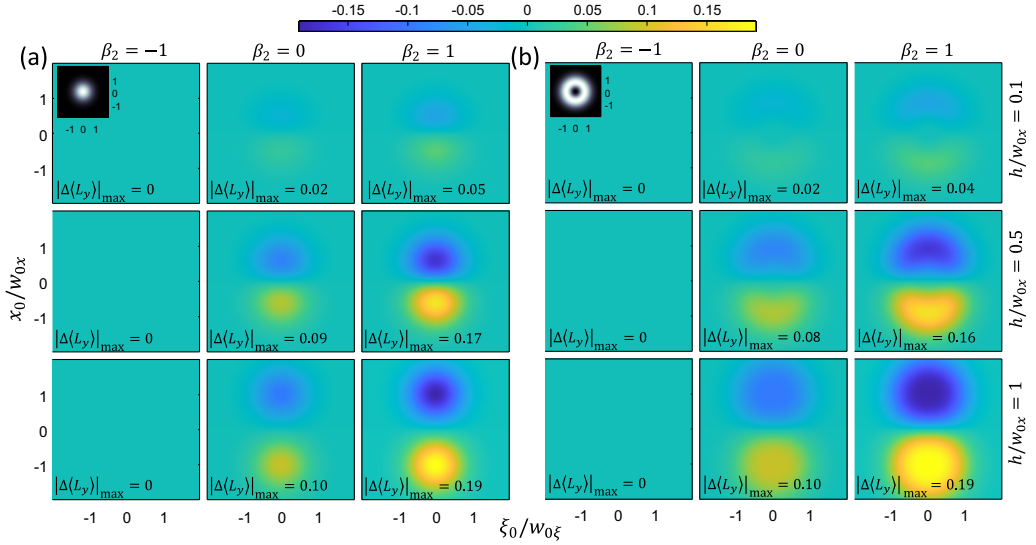

FIG. 2. Plots of analytic solutions [Eqs. (6a) and (6b)] of $\Delta\langle L_y\rangle$ vs (x_0, ξ_0) for the spatiotemporal phase shift $\Delta\phi_p(x,\xi)$ of Eq. (4) applied to (a) a Gaussian pulse $A_{\mathrm{G}}(x,\xi)$ [Eq. (5a)] and to (b) an $l = 1$ STOV pulse $A_{\mathrm{STOV}}(x,\xi)$ [Eq. (5b)]; x_0 and ξ_0 are the central space location and turn-on time of the perturbation. In Eq. (4), we choose $\Delta\phi_{p0} = -0.5$ to model the plasma generated by optical field ionization (OFI) of air.

The effect of the perturbation on an $l = 1$ STOV pulse is plotted in Fig. 2(b). Based on our prior discussion, it is not surprising that the plots are qualitatively similar to those for $l = 0$ in Fig. 2(a), with similar values of maximum OAM transfer $|\Delta\langle L_y\rangle|_{\max}$. For a phase perturbation with $|\Gamma(x,\xi)| = 1$, Eq. (3) shows that $\Delta\langle L_y\rangle$ does not depend on $\phi_s(x,\xi)$, the phase winding of the initial pulse. Detailed differences between Figs. 2(a) and 2(b) arise from the different energy-density distributions $|A_s(x,\xi)|^2$ for Gaussian and STOV pulses.

For $\beta_2 = -1$, $\Delta\langle L_y\rangle = 0$ in all cases. In such a negatively dispersive material, the spatiotemporal pulse shape is preserved because the dispersion in time matches the amplitude and sign of diffraction in space. The effect of any spatiotemporal torque applied to the pulse is zero, because the effective forces applied at the end of the lever arm are balanced.

We now address the effect of a non-energy-conserving pure amplitude perturbation on pulses with and without initial transverse OAM. We place the perturbation $\Gamma(x,\xi) = 1 - \exp[-(x/h)^8]$ at the beam waist ($z = 0$) of $l = 1$ STOV and Gaussian pulses described by Eqs. (5a) and (5b), with $w_{0x} = w_{0\xi} = 100$ μm, and $2h = 100$ μm. This models a steady-state obstruction in the pulse propagation path such as a solid wire of diameter $2h$ centered at $x = 0$, which would remove pulse energy by a combination of scattering and absorption. Shown in Fig. 3(a) are the unperturbed spatiotemporal intensity profiles $I_s(x,\xi) = |E_s(x,\xi)|^2$ for the STOV and Gaussian pulses at $z = 0^-$ followed by the perturbed pulses $I_{sp}(x,\xi) = |E_{sp}(x, y = 0, \xi; z)|^2$ propagating from $z = 0$ to $z = 2z_{0x}$. These are computed by forward-propagating the electric and magnetic fields $\mathbf{E}_{sp}(x,y,\xi;z)$ and $\mathbf{H}_{sp}(x,y,\xi;z)$ from $z = 0$ using our unidirectional pulse propagation code YAPPE (yet another pulse propagation effort) (see Appendix B). The z-dependent change in transverse OAM $\Delta\langle L_y\rangle_z$ is calculated directly from the fields using Eq. (1b) and plotted in Fig. 3(b) as points every $0.1z_{0x}$. In both cases, as expected, $\Delta\langle L_y\rangle_z$ remains constant after the perturbation, owing to the conservation of L_y. It is seen that only the STOV pulse has its transverse OAM per photon changed. This is predicted by Eq. (3): The second term contributes only if $L_y\phi_s \neq 0$ [the first term in Eq. (3) is zero because this is a pure amplitude perturbation]. Note that even though the perturbation is on the beam axis at $x = 0$, $\Delta\langle L_y\rangle$ is still nonzero because energy is removed from the pulse at a specific location, imposing a new spatiotemporal distribution of the remaining energy and thus a new transverse OAM per photon. Changing the x position of the wire will change $\Delta\langle L_y\rangle$ through new spatiotemporal distributions of the remaining energy. The constant solid line overlaid on the points is determined by a calculation of $\Delta\langle L_y\rangle_{z=0}$ using Eq. (1a) and agrees with the direct field calculation.

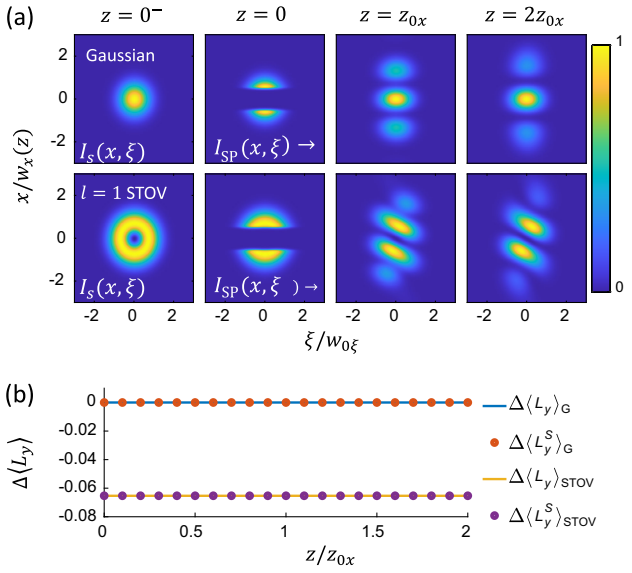

FIG. 3. Effect of a non-energy-conserving pure amplitude perturbation $\Gamma(x,\xi) = 1 - \exp[-(x/h)^8]$ on pulses with and without transverse OAM. (a) Preperturbation $l = 1$ STOV and Gaussian pulse intensities $|E_s(x,\xi)|^2$ at $z = 0^-$, followed by the pulse intensity evolution $|E_{sp}(x, y = 0, \xi; z)|^2$ from $z = 0$ to $z = 2z_{0x}$ determined by **E** and **H** field propagation computed by YAPPE (Appendix B). Here, $2h = 100$ μm and $w_{0x} = w_{0\xi} = 100$ μm. (b) Change in transverse OAM per photon vs z ($\Delta\langle L_y\rangle_z$) for the Gaussian and STOV pulses calculated directly from the fields using Eq. (1b) (points) and calculated using Eq. (1a) (solid lines).

To conclude this section, it is important to make a connection to the generation of transverse OAM-carrying pulses using our $4f$-pulse shaper [14–16]. The shaper is a complex device that generates STOVs by applying torque in the spatiospectral domain to zero-OAM Gaussian input pulses. One realization of the pulse shaper has a π-step phase plate in its Fourier $[(x,\omega)]$ plane and generates donut-shaped STOV pulses in the near field [16]. The phase jump in the (x,ω) plane $\Delta\varphi_p(x,\omega) = \arg[\tilde{E}_{sp}(x,\omega)]$, where $\tilde{E}_{sp}$ is the time Fourier transform of the shaper-perturbed pulse, plays a role analogous to the phase change $\Delta\phi_p(x,\xi)$ in the spatiotemporal domain. However, because we exist in a spatiotemporal rather than a spatiospectral world, with clocks marking time as the dynamical running parameter, it is spatiotemporal perturbations that naturally appear in light-matter interactions. It is spatiotemporal perturbations that are the subject of this paper.

IV. EXPERIMENTAL SETUP

The physical insight provided by the calculations of Sec. III led to our experimental design. To impart a spatiotemporal torque on an optical pulse via a perturbation $\Gamma(x,\xi) = |\Gamma(x,\xi)|e^{i\Delta\phi_p(x,\xi)}$, we impose a spatiotemporal refractive-index perturbation in the propagation medium.

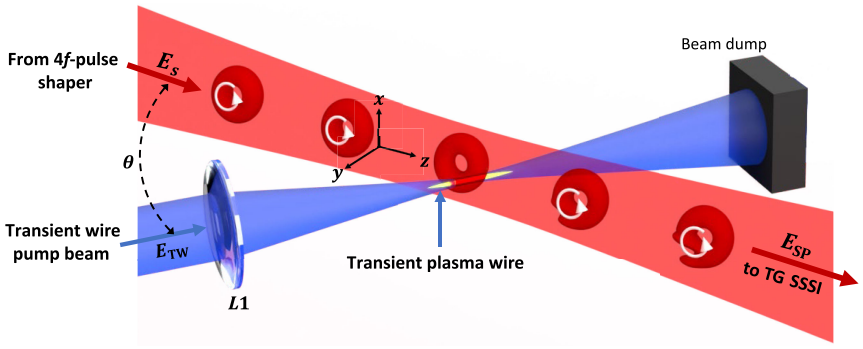

FIG. 4. Configuration for measuring the effect of a transient phase perturbation on field E_s (from a $4f$ -pulse shaper) imposed by the ultrafast OFI plasma induced by field E_{TW}. This OFI plasma is the transient wire. The perturbed pulse E_{sp} and unperturbed pulse E_s (E_{TW} off) are measured by TG-SSSI [17]. The angle between the beams is $\theta = 18.5°$. A detailed experimental diagram is shown in Appendix C.

This is accomplished by using a separate pulse to generate an ultrafast optical-field ionization (OFI) air plasma at a controllable spacetime location; we call this spatiotemporal structure a "transient wire." As borne out by measurements and propagation simulations, the low-density plasma in the transient wire is dominantly a phase perturbation, with negligible energy removed from the pulse, effectively $|\Gamma(x,\xi)| = 1$. The transient wire has an ultrafast rise time and a narrow spatial width governed by the OFI rate, and a long lifetime governed by nanosecond-timescale recombination: The spatiotemporal phase shift $\Delta\phi_p(x,\xi)$ is therefore well described by Eq. (4) or by a more realistic perturbation with smoothed step transitions

$$\Delta\phi_p(x,\xi) = \frac{1}{2}\Delta\phi_{p0}\{1+\mathrm{erf}[\sqrt{2}(\xi-\xi_0)/h_\xi]\} \times \exp\{-[(x-x_0)/h_x]^8\}, \quad (7)$$

where the exponent 8 corresponds to the number of 800-nm photons for multiphoton ionization of air, specifically oxygen. (Pure amplitude perturbations are investigated with simulations in Fig. 3.)

Figure 4 is a schematic diagram of the transient wire experiment; a more detailed diagram is presented in Appendix C. Pulse E_s (red beam), either a Gaussian or $l = 1$ STOV pulse from a $4f$-pulse shaper [14–16], propagates through air and is intersected by a focused secondary pulse E_{TW} (blue beam) which generates an ultrafast-rise-time OFI plasma—the transient wire—at an adjustable spacetime location with respect to E_s. After the interaction, the perturbed pulse E_{sp} is relay imaged from 3 mm past the interaction plane (to avoid nonlinear distortion in the imaging) to our TG-SSSI diagnostic [17], which extracts its spatiotemporal amplitude and phase. With E_{TW} turned off, TG-SSSI measures the spatiotemporal amplitude and phase of the unperturbed pulse E_s. Five synchronized beams are needed for this experiment, which are obtained by splitting the output beam of a 1-kHz repetition-rate Ti:sapphire laser ($\lambda_0 = 800$ nm, 40 fs) to give (1) an input pulse to the $4f$-pulse shaper, with output pulse E_s (9.5 μJ, variable pulse width), (2) a focused transient wire beam E_{TW} (250 μJ, 40-fs FWHM, spot size $w_{TW} = 40$ μm) that intersects the E_s beam at $\theta = 18.5°$, and (3) three pulses for TG-SSSI: twin probe and reference supercontinuum (SC) pulses E_{pr} and E_{ref} (with bandwidth $\Delta\lambda_{SC} \sim 160$ nm centered at $\lambda_{SC} = 630$ nm) plus a spatial interferometry reference pulse $\mathcal{E}_i$ (5.5 μJ after 3-nm bandpass filter centered at 800 nm). The angle $\theta = 18.5°$ is chosen to allow angular separation of the beams to direct E_{sp} to the TG-SSSI diagnostic, and for sufficient spatial overlap of $\Delta\phi_p(x,\xi)$ along the propagation path of E_s.

V. RESULTS AND DISCUSSION

An example of the transient wire perturbation of an $l = 1$ STOV pulse $E_s(x,\tau)$ is shown in Fig. 5, where here we use the time coordinate relative to the pulse center $\tau = \xi/v_g$, and $(x,\tau) = (0,0)$ is taken as the spatiotemporal energy center of E_s. Figures 5(a)–5(c) show, respectively, the unperturbed $l = 1$ STOV pulse intensity $|E_s|^2$ (E_{TW} off), the perturbed pulse intensity $|E_{sp}|^2$ (E_{TW} on), and the transient-wire-induced phase shift $\Delta\phi_p(x,\tau) = \arg(E_{sp}) - \arg(E_s)$, all extracted using TG-SSSI [16,17]. The overlaid dashed red line shows the x location of the perturbation, which is placed near the top of E_s (at $x_0 = 120$ μm) to obtain appreciable $\Delta\langle L_y\rangle$, as motivated by the simulations in Fig. 2(b). The plots represent a $\Delta y \sim 10$ μm slice of E_s and E_{sp} in the y direction, normal to the x-τ plane of the plots, where Δy is the width of the imaging spectrometer slit used in TG-SSSI (see Ref. [17] and Appendix C).

From Fig. 5(c), the maximum phase shift induced by the OFI plasma is $\Delta\phi_{p0} = -0.45$, where E_{TW} was delayed so that the half-maximum phase shift $\Delta\phi_{p0}/2$, which defines the perturbation onset time τ_0, occurred for $\tau_0 = 0$. From nonlinear least-squares fitting of measured $\Delta\phi_p(x,\tau)$ to Eq. (7), we extract the phase-shift rise time $h_\tau = h_\xi/v_g \sim 44$ fs and spatial half-width at $1/e$ maximum $h_x \sim 40$ μm

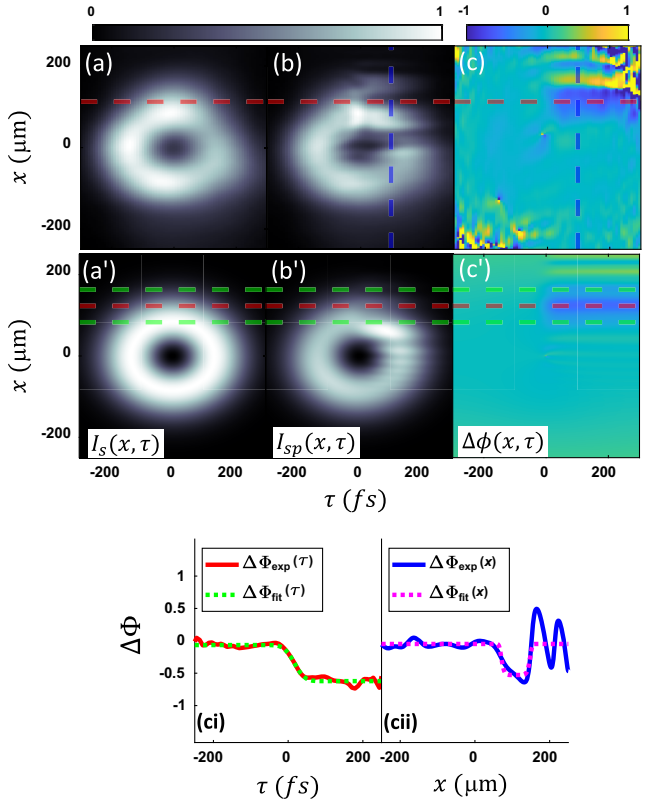

FIG. 5. (a) TG-SSSI measured $I_s = |\mathbf{E}_s(x,\tau)|^2$ (transient wire off). (b) and (c) TG-SSSI measured $|\mathbf{E}_{sp}(x,\tau)|^2$ and $\Delta\phi_p(x,\tau)$ (in rad) (transient wire on). (a′)–(c′) corresponding simulated $I_s^{sim} = |\mathbf{E}_s^{sim}(x,\tau)|^2$, $I_{sp}^{sim} = |\mathbf{E}_{sp}^{sim}(x,\tau)|^2$, and $\Delta\phi_p^{sim}(x,\tau)$. (ci) Lineout of (c) along dashed red line (solid red) and fit (dotted green). (cii) Lineout of (c) along dashed blue line (solid blue) and fit (dotted pink). The fit curve neglects the oscillations on the right, which are due to the imaging plane being 3 mm past the interaction (see text). The fits in (ci) and (cii) are to $\Delta\phi_p^{sim}(x,\tau) = \frac{1}{2}\Delta\phi_{p0}(1+\mathrm{erf}[\sqrt{2}(\tau-\tau_0)/h_\tau])\exp\{-[(x-x_0)/h_x]^8\}$, giving $h_\tau = h_\xi/v_g = 44$ fs and $h_x = 40\,\mu$m. In (ci) $x = 120$ μm $(=x_0)$, and in (cii) $\tau = 100$ fs.

with data lineouts overlaid with fits in Figs. 5(c(i)) and 5(c(ii)). The peak phase shift corresponds to an OFI plasma density $\Delta N_e = |\Delta\phi_{p0}|N_{cr}\lambda_0/2\pi L \approx 5\times10^{17}$ cm^{-3}, where $N_{cr} = 1.7\times10^{21}$ cm^{-3} is the critical density at $\lambda_0 = 800$ nm and $L = 2w_{TW}/\sin\theta \sim 250$ μm is the OFI plasma length experienced by E_s. It is seen in Fig. 5(b) that an amplitude modulation feature lies below the dashed red line, starting near $\tau = 0$. This modulation is the diffractive consequence of the OFI-induced phase perturbation and develops during the 3 mm of propagation from the interaction location to the TG-SSSI object plane. This effect is borne out by the simulations of Figs. 5(a′)–(c′) [performed using YAPPE (Appendix B)], which show that similar diffractive modulations occur equidistantly above and below the dashed red line, but have no effect on the change in angular momentum of the pulse. Figure 5(a′) shows the simulated unperturbed pulse $|E_s^{sim}|^2$ (E_{TW} off) and Fig. 5(b′) shows the perturbed pulse $|E_{sp}^{sim}|^2$ (E_{TW} on), both 3 mm past the intersection with E_{TW}. Here, the perturbation by E_{TW} is simulated by imposing on E_s^{sim} the perturbation $\Gamma(x,\tau) = |\Gamma(x,\tau)|e^{i\Delta\phi_p(x,\tau)}$, with $|\Gamma(x,\tau)| = 1$ and $\Delta\phi_p^{sim}(x,\tau)$ from Eq. (7), using h_τ and h_x derived from the fit discussed above. The red and green horizontal dashed lines in Figs. 5(a′)–5(c′) mark the center $(x = x_0)$ and $\pm h_x$ edges of $\Delta\phi_p^{sim}(x,\tau)$.

In our main experiment, the results of which are shown in Fig. 6, we varied the spatiotemporal torque on both STOV and Gaussian pulses by scanning the transient wire onset time τ_0. For torquing the STOV pulse, we spatially placed the wire near the top and bottom edges of the pulse, $x_0 = \pm120$ μm [Figs. 6(a) and 6(b)] and at $x_0 = 60$ μm for the Gaussian pulse [Fig. 6(c)]. The onset time was scanned from −200 to 800 fs in steps of $\Delta\tau_0 \sim 66$ fs, and the TG-SSSI-extracted complex spatiotemporal fields $E_s(x,\tau)$ and $E_{sp}(x,\tau)$ were then used to determine $\Delta\langle L_y\rangle$ at each delay using Eqs. (1a) and 1(b), which we label as $\Delta\langle L_y\rangle_{1a}$ and $\Delta\langle L_y\rangle_{1b}$. In Eq. (1a), we use the STOV OAM operator $L_y = -i\xi\partial/\partial x$ (for $\beta_2 = 0$) and the measured $\mathbf{E}_{s,sp}(x,\xi)$ fields, while in Eq. (1b), the $\mathbf{H}_{s,sp}(x,\xi)$ fields are calculated as the 2D inverse Fourier transforms of $\tilde{\mathbf{H}}_{s,sp}(k,\omega) = (c/\omega)\mathbf{k}\times\tilde{\mathbf{E}}_{s,sp}(\mathbf{k},\omega)$, where $\tilde{\mathbf{E}}_{s,sp}(\mathbf{k}-\mathbf{k}_0,\omega)$ is the discrete 2D Fourier transform of the measured $\mathbf{E}_{s,sp}(x,\xi)$ fields and $\mathbf{k}_0 = k_0\hat{\mathbf{z}}$ is the pulse central wave number.

The top two rows in Figs. 6(a)–6(c) plot $I_{sp}(x,\tau) = |\mathbf{E}_{sp}(x,\tau)|^2$ and $\Delta\phi_p(x,\tau) = \arg[E_{sp}(x,\tau)] - \arg[E_s(x,\tau)]$, with all amplitude and phase data extracted from raw TG-SSSI frames averaged over 500–750 shots. The lower panels plot $\Delta\langle L_y\rangle_{1a}$ and $\Delta\langle L_y\rangle_{1b}$ versus the transient wire onset delay. These plots are in excellent agreement, confirming that our expression for the transverse OAM operator L_y [Ref. [22] and Eq. (2)] is correct. Overlaid in Figs. 6(a)–(c) are curves for $\Delta\langle L_y\rangle_{theory}$, using Eqs. (6a) and (6b) for $\Delta\langle L_y\rangle_G$ and $\Delta\langle L_y\rangle_{STOV}$. Agreement with the experimental results is excellent. In each experiment in Fig. 6, the measured experimental parameters are slightly different. These are listed in the figure caption and are incorporated into the expressions for $\Delta\langle L_y\rangle_G$ and $\Delta\langle L_y\rangle_{STOV}$.

The results of Fig. 6 confirm our Sec. III theory: Once the OFI plasma phase transient is shifted away from the pulse envelope, $\Delta\langle L_y\rangle \to 0$. To impart spatiotemporal torque and a change in transverse OAM, the perturbation transient must temporally overlap with the pulse energy-density distribution. Refractive-index transients with timescales much longer than the pulse temporal envelope have little effect on the transverse OAM of a pulse. In general, irrespective of its spatial location or peak amplitude, the more imbalanced a transient spatiotemporal perturbation is across the temporal center of energy of an optical pulse, the greater effect it has on changing the transverse OAM.

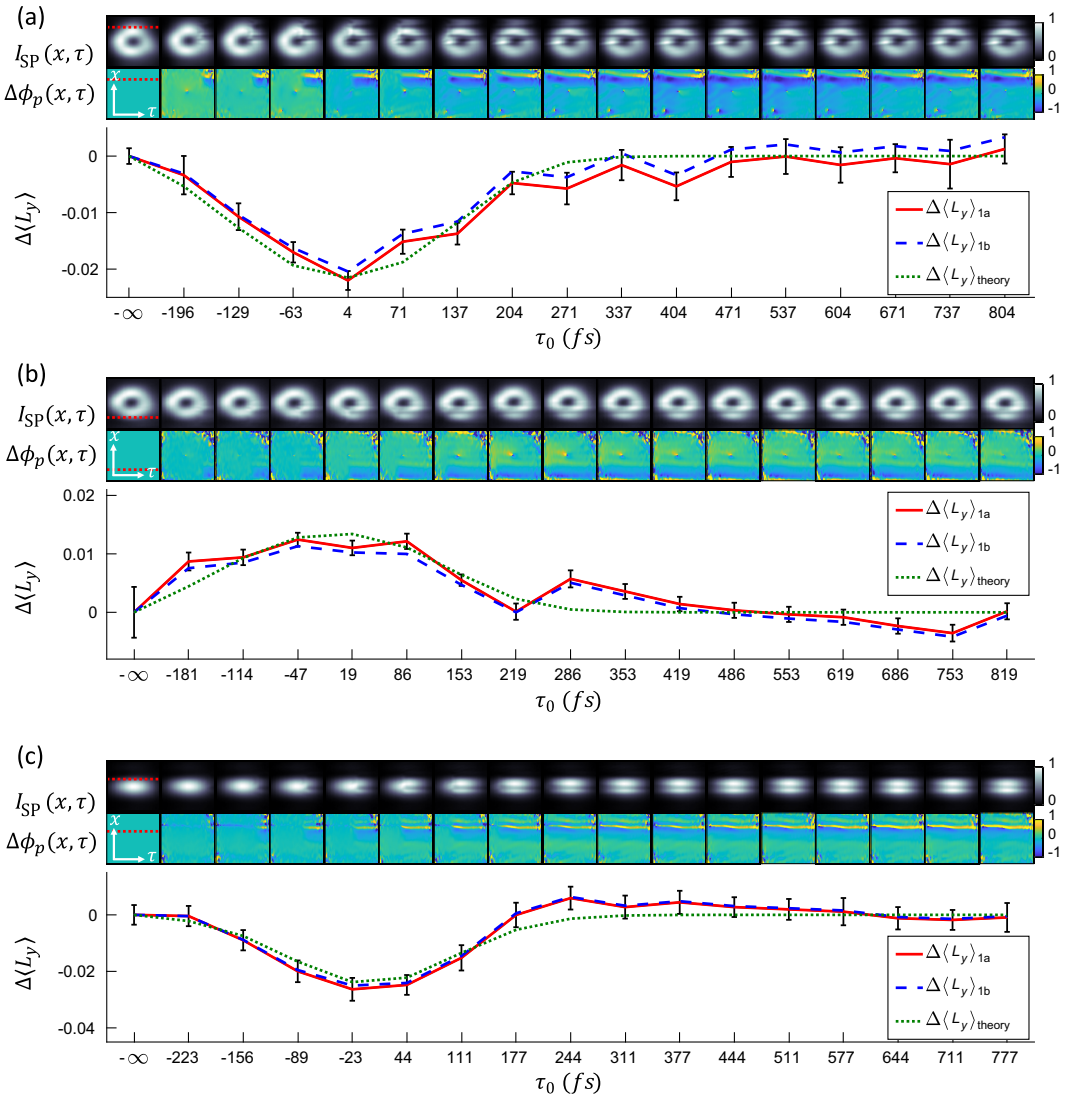

FIG. 6. Effect of transient wire onset time τ_0 on changing the transverse OAM of STOV and Gaussian pulses. Onset time is scanned between −200 and 800 fs in $\Delta\tau_0 = 66$ fs steps. (a) $l = 1$ STOV pulse, with transient wire centered at $x_0 = +120$ μm; (b) $l = 1$ STOV pulse, with transient wire centered at $x_0 = -120$ μm; (c) Gaussian pulse ($l = 0$), with transient wire centered at $x_0 = 60$ μm. The top two rows in (a)–(c) are $I_{sp}(x,\tau) = |E_{sp}(x,\tau)|^2$ and $\Delta\phi_p(x,\tau) = \arg(E_{sp}) - \arg(E_s)$ (in rad), where $E_s(x,\tau)$ and $E_{sp}(x,\tau)$ are the unperturbed and perturbed complex fields extracted from TG-SSSI measurements. The spatial location of the perturbation is indicated by the red dotted lines. The bottom panels in (a)–(c) plot $\Delta\langle L_y\rangle_{1a}$ and $\Delta\langle L_y\rangle_{1b}$, which are the change in spatiotemporal OAM per photon computed by inserting the measured E_s and E_{sp} into Eq. (1a), and the **E** and **H** fields computed from them into Eq. (1b). The error bars are the ± standard deviation over 500–750 shots of extracted data. Overlaid in (a)–(c) is $\Delta\langle L_y\rangle_{theory}$ calculated using Eqs. (6a) and (6b), in which we use measured and fit quantities. The FWHM of $\Delta\langle L_y\rangle_{theory}$ in (a) and (b) is 280 fs. For $\Delta\langle L_y\rangle_{theory}$ in panel (a) $\Delta\phi_{p0} = -0.45$, $w_{0x} = 120$ μm, $w_{0\xi} = 56$ μm, $h = 40$ μm, $x_0 = 120$ μm). For $\Delta\langle L_y\rangle_{theory}$ in panel (b) $\Delta\phi_{p0} = -0.21$, $w_{0x} = 110$ μm, $w_{0\xi} = 56$ μm, $h = 40$ μm, $x_0 = -120$ μm. For $\Delta\langle L_y\rangle_{theory}$ in panel (c) $\Delta\phi_{p0} = -0.31$, $w_{0x} = 100$ μm, $w_{0\xi} = 61$ μm, $h = 40$ μm, $x_0 = 60$ μm. The "−∞" mark on the time axes refers to the $\xi_0 \to -\infty$ limit of $\Delta\langle L_y\rangle_{theory}$.

VI. CONCLUSIONS

We have demonstrated that the transverse OAM per photon of an electromagnetic pulse can be changed only by a transient phase perturbation comparable to the pulse envelope and overlapping with it, or by a non-energy-conserving amplitude perturbation if the pulse already has transverse OAM density. Our half-integer theory of STOV pulse OAM [22] is in excellent agreement with our experiments and with propagation simulations that directly use the **E** and **H** fields. The experiments of this paper, in which spatiotemporal torques transiently overlapped the short pulses to which they were applied, would not have

been possible without our ability to extract STOV pulse amplitude and phase, and small changes in transverse OAM, using our high-bandwidth, high time- and space-resolution single-shot technique, TG-SSSI [17].

The concept of spatiotemporal torque introduced in this paper, provides insight into the dynamics leading to changes in transverse OAM: The effective force manifested as a spatiotemporal phase gradient supplied by the perturbation is weighted by the spacetime lever arm and the electromagnetic energy-density distribution. If the initial field is a STOV pulse with zero energy density at the singularity (an "edge-first flying donut" [16]), spatiotemporal torquing can be analogized by mechanical torque on a rotating hoop, where maximum change in OAM is obtained by applying force at the outer rim, where the product of lever arm and mass density is maximum. However, unlike in the mechanical case, a spatiotemporal torque applied to an optical pulse changes the OAM of all particles (photons) identically. The other way to change transverse OAM is to remove energy from a pulse already containing transverse OAM density; this can be accomplished by a non-energy-conserving amplitude perturbation. This imposes a new spatiotemporal distribution of the remaining energy and thus a new transverse OAM per photon. Here, the mechanical analogy is location-specific mass removal from a spinning wheel.

Our results point the way to methods of distortion-free encoding of information in transverse OAM, for example, in propagation through turbulent atmosphere. The shortest transient timescale for turbulent refractive-index fluctuations in the atmosphere is a few milliseconds [38], at least 10 orders of magnitude longer than a 100 fs pulse, so air turbulence acts as a weak stationary perturbation with no effect on the expectation value of transverse OAM per photon. While the turbulence-induced spatial phase shifts can manifest as transverse (xy) spatial distortion of the beam, the encoded spatiotemporal phase structure makes possible the extraction of time-based information with fast retrieval schemes.

ACKNOWLEDGMENTS

The authors thank Nishchal Tripathi for technical assistance. This work is supported by the Air Force Office of Scientific Research (Grant No. FA9550-21-1-0405), Office of Naval Research (Grants No. N00014-17-1-2705 and No. N00014-20-1-2233), and the National Science Foundation (Grant No. PHY2010511).

APPENDIX A: TRANSVERSE ORBITAL ANGULAR MOMENTUM OF LIGHT

1. Choice of origin in the calculation of intrinsic OAM

In the interaction of OAM-carrying light with matter, only the intrinsic OAM carried by photons is of physical significance. Direct calculation of the intrinsic OAM of an electromagnetic field depends on the correct choice of origin. Recently, this has been a point of discussion in the context of STOV pulses with transverse OAM [34,39]. Here we show that the correct choice of origin for directly isolating the intrinsic part of OAM is the electromagnetic energy centroid. This applies to longitudinal, transverse, or any other orientation of OAM.

Consider the electromagnetic angular momentum (AM) quantity $\boldsymbol{\mathcal{L}}$ evaluated with respect to an arbitrary position $\mathbf{r}_c$, where the integral is over all space. In general, this includes OAM and spin angular momentum

$$\boldsymbol{\mathcal{L}} = (4\pi c)^{-1} \int d^3\mathbf{r}(\mathbf{r}-\mathbf{r}_c)\times(\mathbf{E}\times\mathbf{H}) \text{ or}$$

$$\boldsymbol{\mathcal{L}} = (4\pi c)^{-1} \int d^3\mathbf{r}\ \mathbf{r}\times(\mathbf{E}\times\mathbf{H}) - \mathbf{r}_c\times\mathbf{v}_{\mathrm{CE}}U/c^2. \quad \text{(A1)}$$

Here, we use the general relation, for both massless and massive particles, between total linear momentum $\mathbf{P}$ and the velocity of the center of energy $\mathbf{v}_{\mathrm{CE}}$,

$$\mathbf{v}_{\mathrm{CE}}U/c^2 = \mathbf{P} = (4\pi c)^{-1}\int d^3\mathbf{r}(\mathbf{E}\times\mathbf{H}), \quad \text{(A2)}$$

where here $U = (16\pi)^{-1}\int d^3\mathbf{r}(|\mathbf{E}|^2+|\mathbf{H}|^2)$ is the total pulse energy. In vacuum $|\mathbf{v}_{\mathrm{CE}}| = c$, and in a dispersive medium $|\mathbf{v}_{\mathrm{CE}}| = v_g$.

Consulting Fig. 7, consider an arbitrary lab-frame origin from which we take $\mathbf{r}_c = \mathbf{r}_{\mathrm{CE}} = \mathbf{r}_{\mathrm{CE},\perp} + \mathbf{v}_{\mathrm{CE}}(t-t_0)$, where $\mathbf{r}_{\mathrm{CE},\perp}$ is a vector from the origin to the center-of-energy trajectory and orthogonal to it. Then Eq. (A1) becomes

$$\begin{aligned}\boldsymbol{\mathcal{L}} &= (4\pi c)^{-1}\int d^3\mathbf{r}\ \mathbf{r}\times(\mathbf{E}\times\mathbf{H}) - \mathbf{r}_{\mathrm{CE}}\times\mathbf{P}\\ &= \mathbf{L}_{\mathrm{tot}} - \mathbf{L}_{\mathrm{ext}}, \end{aligned}\quad \text{(A3)}$$

where the first term is the time-invariant total AM $\mathbf{L}_{\mathrm{tot}}$, and we identify the second term as the arbitrary extrinsic OAM $\mathbf{L}_{\mathrm{ext}} = \mathbf{r}_{\mathrm{CE}}\times\mathbf{P} = \mathbf{r}_{\mathrm{CE},\perp}\times\mathbf{P}$, which is also invariant because $d\mathbf{L}_{\mathrm{ext}}/dt = d\mathbf{r}_{\mathrm{CE}}/dt\times\mathbf{P} = 0$. Thus, we identify

$$\boldsymbol{\mathcal{L}} = (4\pi c)^{-1}\int d^3\mathbf{r}(\mathbf{r}-\mathbf{r}_{\mathrm{CE}})\times(\mathbf{E}\times\mathbf{H}) = \mathbf{L}_{\mathrm{int}} \quad \text{(A4)}$$

as the intrinsic electromagnetic angular momentum.

Note that Eq. (A4) is general and can apply to both longitudinal and transverse OAM (STOV) pulses as sketched in Fig. 7. A propagating pulse with longitudinal OAM, as shown in Fig. 7(a), has its intrinsic OAM directly calculated using Eq. (A4) with $\mathbf{r}_{\mathrm{CE}} = \mathbf{v}_{\mathrm{CE}}(t-t_0)$. Monochromatic fields with longitudinal OAM can be

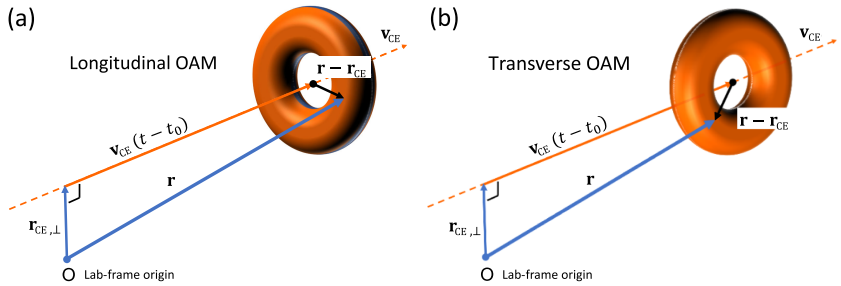

FIG. 7. (a) Pulse with longitudinal OAM propagating at center-of-energy velocity $\mathbf{v}_{CE}$. Monochromatic, "infinitely long" pulses can be viewed as this pulse stretched in the $\pm\mathbf{v}_{CE}$ directions. In that case, the calculation of intrinsic OAM is done using $\mathbf{L}_{int} = (4\pi c)^{-1}\int d^3\mathbf{r}(\mathbf{r}-\mathbf{r}_{CE})\times(\mathbf{E}\times\mathbf{H})$ with no reference to $\mathbf{v}_{CE}$. (b) STOV pulse (with transverse OAM) propagating at center-of-energy velocity $\mathbf{v}_{CE}$. All coordinates in (a) and (b) are in the lab frame.

viewed as pulses with bandwidth narrowed to zero and "infinitely stretched" in the $\pm\mathbf{v}_{CE}$ directions. Then the integral becomes one purely in the plane transverse to $\mathbf{v}_{CE}$, but without reference to $\mathbf{v}_{CE}$. In the case of transverse OAM-carrying pulses, as shown in Fig. 7(b), one uses $\mathbf{r}_{CE} = \mathbf{v}_{CE}(t-t_0)$. When intrinsic transverse OAM is evaluated with respect to $\mathbf{r}_{CE}$, the total transverse linear momentum perpendicular to propagation vanishes, $\mathbf{P}_\perp = 0$, as is also the case when calculating intrinsic longitudinal OAM [40].

In light of these results, we now consider recent work by Bliokh [34] and Porras [39]. For the case of a symmetric pulse propagating along z with respect to the origin $(x,z) = (0,0)$,$\mathbf{v}_{CE} = v_{CE}\hat{\mathbf{z}}$. Inspection of Fig. 7 immediately shows that $\mathbf{r}_{CE,\perp} = 0$ and $\mathbf{L}_{ext} = 0$. However, for exactly these conditions, Ref. [39] calculates $\mathbf{L}_{ext} \neq 0$. In the specific case of a symmetric STOV pulse of topological charge l, Ref. [39] calculates $\mathbf{L}_{ext} = -l/2\hat{\mathbf{y}}$ and then assigns a physical significance to it. However, whatever the value of $\mathbf{L}_{ext}$, it is of no physical consequence; it is an arbitrary quantity having nothing to do with the OAM carried by photons. It plays no role in the exchange of OAM between light and matter.

Regarding Ref. [34], it is asserted that the correct choice of origin when calculating intrinsic OAM is the "photon centroid" $\mathbf{r}_{PC}$, which is defined using the "photon wave function" [41] to be the photon-number density-weighted position. Then one would write $\mathbf{L}_{tot} = \mathbf{L}_{int} + \mathbf{r}_{PC}\times\mathbf{P}$. Applying the time derivative to this equation, and requiring that $\mathbf{L}_{int}$, $\mathbf{L}_{tot}$, and $\mathbf{P}$ be invariant, one must have $d\mathbf{r}_{PC}/dt \times \mathbf{P} = 0$ for AM conservation. However, $d\mathbf{r}_{PC}/dt \neq 0$ for a moving pulse and, in general, $d\mathbf{r}_{PC}/dt \neq \mathbf{v}_{CE}$ (consider, for example, an optical pulse with spatial chirp). Therefore, $d\mathbf{r}_{PC}/dt \times \mathbf{P} \neq 0$, AM is not conserved in the formulation of Ref. [34], and the choice of photon centroid is incorrect. A straightforward mechanical analogy also makes this point: The intrinsic OAM of a composite body, consisting of point particles of varying mass, must be calculated with respect to the center of mass and not the particle number centroid.

2. Conservation of transverse OAM operator L_y under nonparaxial propagation

In Ref. [22], we showed that the transverse OAM operator $L_y = -i(\xi\partial/\partial x + \beta_2 x\partial/\partial\xi)$ was conserved under paraxial propagation. Here, we extend this to the nonparaxial case. We start with the nonparaxial propagation equation for the field envelope $A(\mathbf{r}_\perp, z, t)$,

$$\frac{\partial^2 A}{\partial z^2} + i2k_0\frac{\partial A}{\partial z} = -\nabla_\perp^2 A - i2k_0k_0'\frac{\partial A}{\partial t} + k_0k_0''\frac{\partial^2 A}{\partial t^2}. \tag{A5}$$

Using $\zeta = z$, $\xi = v_g t - z$, $H = -\nabla_\perp^2 + \beta_2\partial^2/\partial\xi^2$, and $p_z^2 = -\partial^2/\partial z^2$, Eq. (A5) becomes

$$\begin{aligned}\frac{\partial A}{\partial\zeta} &= \frac{i}{2k_0}\left[HA - \left(\frac{\partial^2 A}{\partial\zeta^2} - 2\frac{\partial^2 A}{\partial\zeta\partial\xi} + \frac{\partial^2 A}{\partial\xi^2}\right)\right] \\ &= \frac{i}{2k_0}[H - p_z^2]A.\end{aligned} \tag{A6}$$

Then for $\langle L_y\rangle = \langle A|L_y|A\rangle$,

$$\frac{d}{dz}\langle L_y\rangle = \langle\frac{\partial}{\partial z}A|L_y|A\rangle + \langle A|\frac{\partial}{\partial z}L_y|A\rangle + \langle A|L_y|\frac{\partial}{\partial z}A\rangle. \tag{A7}$$

Since L_y does not explicitly depend on z, and since H, L_y, and p_z are all Hermitian, Eq. (A5) becomes

$$\begin{aligned}\frac{d}{dz}\langle L_y\rangle &= \frac{i}{2k_0}\langle A|[H, L_y]|A\rangle + \frac{i}{2k_0}\langle A|[L_y, p_z^2]|A\rangle \\ &= 0,\end{aligned} \tag{A8}$$

because L_y commutes with both H and p_z^2.

3. Assessment of an alternative transverse OAM operator

Recent work by Bliokh [33,34] has asserted that the "canonical" operator for the intrinsic transverse OAM is

$$\pounds_y = -i\left(\xi\frac{\partial}{\partial x} - x\frac{\partial}{\partial \xi}\right), \tag{A9}$$

where x and ξ are as defined earlier. In the formulation of Refs. [33,34], x and ξ are treated on an equal footing, just as x and y are treated in the L_z operator for the longitudinal OAM.

Adoption of $\pounds_y$ assumes unphysical effects, including super- and subluminal energy-density flow around the spatiotemporal vortex singularity in vacuum, and nonconservation [22]. While any valid angular momentum quantity should be conserved with propagation, $\pounds_y$ is not. Namely,

$$\frac{d}{dz}\langle \pounds_y\rangle = \frac{i}{2k_0}\langle [H,\pounds_y]\rangle = k_0^{-1}(1+\beta_2)\left\langle \frac{\partial^2}{\partial x \partial \xi}\right\rangle_{z=0}, \tag{A10}$$

which is nonzero except if $\beta_2 = -1$ (when $L_y \to \pounds_y$) or when there is spatiotemporal field symmetry.

We test the consequences of using $\pounds_y$ against asymmetrically perturbed pulses generated both in simulations and in our experiments. Such fields are generated, as seen in Figs. 5 and 6, when a spatiotemporal perturbation is applied to a symmetric pulse. Here, we simulate an asymmetric perturbation by applying at $z = 0^-$ a phase-only perturbation $\Gamma(x,\xi) = e^{i\Delta\phi_p(x,\xi)}$, with $\Delta\phi_p(x,\xi)$ from Eq. (A7) (with $\Delta\phi_{p0} = -0.5$, $x_0 = -100$ μm, $\xi_0 = 0$, $h_x = 50$ μm, and $h_\xi = 50$ μm) to the Gaussian pulse A_G of Eq. (5a). The transverse OAM of A_G is zero. Nonparaxial propagation evolution of the perturbed field $A_{sp}(x,y,\xi;z) = \Gamma(x,\xi)A_G(x,y,\xi;z)$ is then computed using our code YAPPE (Appendix B). In Fig. 8,

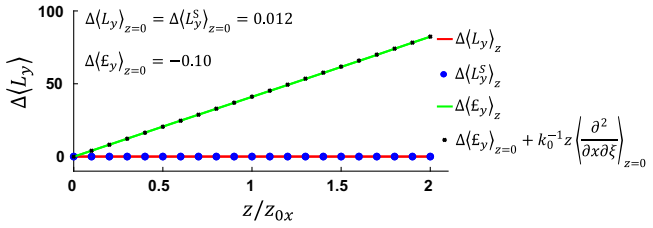

FIG. 8. Propagation evolution of $\Delta\langle L_y\rangle = u_{sp}^{-1}\langle A_{sp}|L_y|A_{sp}\rangle_z$ (red curve) and $\Delta\langle \pounds_y\rangle = u_{sp}^{-1}\langle A_{sp}|\pounds_y|A_{sp}\rangle_z$ (green curve), where the z evolution of $A_{sp}(x,y,\xi;z)$ is nonparaxially computed using our code YAPPE (Appendix B). The perturbation [given by Eq. (7), with $\Delta\phi_{p0} = -0.5$, $x_0 = -100$ μm, $\xi_0 = 0$, $h_x = 50$ μm, and $h_\xi = 50$ μm] is applied to the Gaussian pulse of Eq. (5a), with $w_{ox} = 100$ μm and $w_{0\xi} = 100$ μm. The immediate postperturbation OAM changes are $\Delta\langle L_y\rangle_{z=0} = 0.012$ and $\Delta\langle \pounds_y\rangle_{z=0} = -0.10$. Also plotted are large blue points ΔL_y^S computed using Eq. (1b), with the **E** and **H** fields propagated nonparaxially with YAPPE, and small black points computed as $\Delta\langle \pounds_y\rangle_z = \Delta\langle \pounds_y\rangle_{z=0} + k_0^{-1}z\langle \partial^2/\partial x\partial\xi\rangle_{z=0}$ from integration of Eq. (A10), where $\langle \partial^2/\partial x\partial\xi\rangle_{z=0} = \langle A_{sp}|\partial^2/\partial x\partial\xi|A_{sp}\rangle$ for $A_{sp} = A_{sp}(x,y,\xi;z=0)$.

we plot $\Delta\langle L_y\rangle_z = u_{sp}^{-1}\langle A_{sp}|L_y|A_{sp}\rangle_z$ and $\Delta\langle \pounds_y\rangle_z = u_{sp}^{-1}\langle A_{sp}|\pounds_y|A_{sp}\rangle_z$ as a function of the propagation distance z. The immediate postperturbation values $\Delta\langle L_y\rangle_{z=0}$ and $\Delta\langle \pounds_y\rangle_{z=0}$ are shown in the figure; these differ. It is clear that $\Delta\langle L_y\rangle_z$ is conserved with propagation, while $\Delta\langle \pounds_y\rangle_z$ is not. The divergence of $\Delta\langle \pounds_y\rangle_z$ is predicted by Eq. (A10) and is a consequence of the noncommutation of $\pounds_y$ and the propagation operator H. This increase is linear in z, with slope $d\langle \pounds_y\rangle/dz = k_0^{-1}\langle \partial^2/\partial x\partial\xi\rangle_{z=0}$, and is in excellent agreement with $\Delta\langle \pounds_y\rangle_z = u_{sp}^{-1}\langle A_{sp}|\pounds_y|A_{sp}\rangle_z$. Calculating the change in transverse OAM using Eq. (1b), with the **E** and **H** fields propagated nonparaxially by the YAPPE simulation, gives the blue points labeled as $\Delta\langle L_y^S\rangle_z$; these agree with $\Delta\langle L_y\rangle_z$.

Note that nonconservation of $\langle \pounds_y\rangle$ is independent of choice of origin, whether it is the pulse center of energy $\mathbf{r}'_{sp}$ (as in Fig. 8) or the photon centroid [34], so $\pounds_y$ cannot be corrected with extrinsic OAM contributions. This is because nonconservation of $\pounds_y$ is caused by the inclusion, even in vacuum, of a nonzero linear momentum density $p_\xi = -i\partial/\partial\xi$. As the propagating pulse spatially (transversely) diffracts, with its width in x increasing, the contribution of xp_ξ to $\pounds_y$ increases and $\langle A_{sp}|\pounds_y|A_{sp}\rangle_z$ unavoidably increases with propagation. There are circumstances, not involving pulse propagation, where $\pounds_y$ is appropriate to use. One such example is a vortex stationary in the lab frame [31,32,42], whose transverse OAM, say, along $\hat{\mathbf{y}}$, can be described in x-z space coordinates.

Finally, we directly compare the predictions of Refs. [33,34] against our experimental results. Figure 9 replots the curves of Fig. 6 and overlays $\Delta\langle \pounds_y\rangle$, where the latter is computed using Eq. (1a), with the complex fields provided by the TG-SSSI measurements. The results deviate greatly from the three other curves. We therefore conclude, on both theoretical and experimental grounds, that $\pounds_y$ is an incorrect operator for transverse spatiotemporal OAM. Calculations in recent work [39] support our results for intrinsic transverse OAM [22].

4. Effect of a spatiotemporal perturbation on transverse OAM

The expectation values of L_y per photon for the unperturbed and perturbed pulses $A_s(x,\xi) = |A_s(x,\xi)|e^{i\phi_s(x,\xi)}$ and $A_{sp}(x,\xi) = \Gamma(x,\xi)A_s(x,\xi) = |\Gamma(x,\xi)|e^{i\Delta\phi_p(x,\xi)}A_s(x,\xi)$ are

$$\langle L_y\rangle_{s,sp} = u_{s,sp}^{-1}\langle E_{s,sp}|L_y|E_{s,sp}\rangle. \tag{A11}$$

This gives

$$\langle L_y\rangle_s = u_s^{-1}\int dx d\xi |A_s|^2\left(\xi\frac{\partial\phi_s}{\partial x} + \beta_2 x\frac{\partial\phi_s}{\partial\xi}\right) \tag{A12a}$$

and

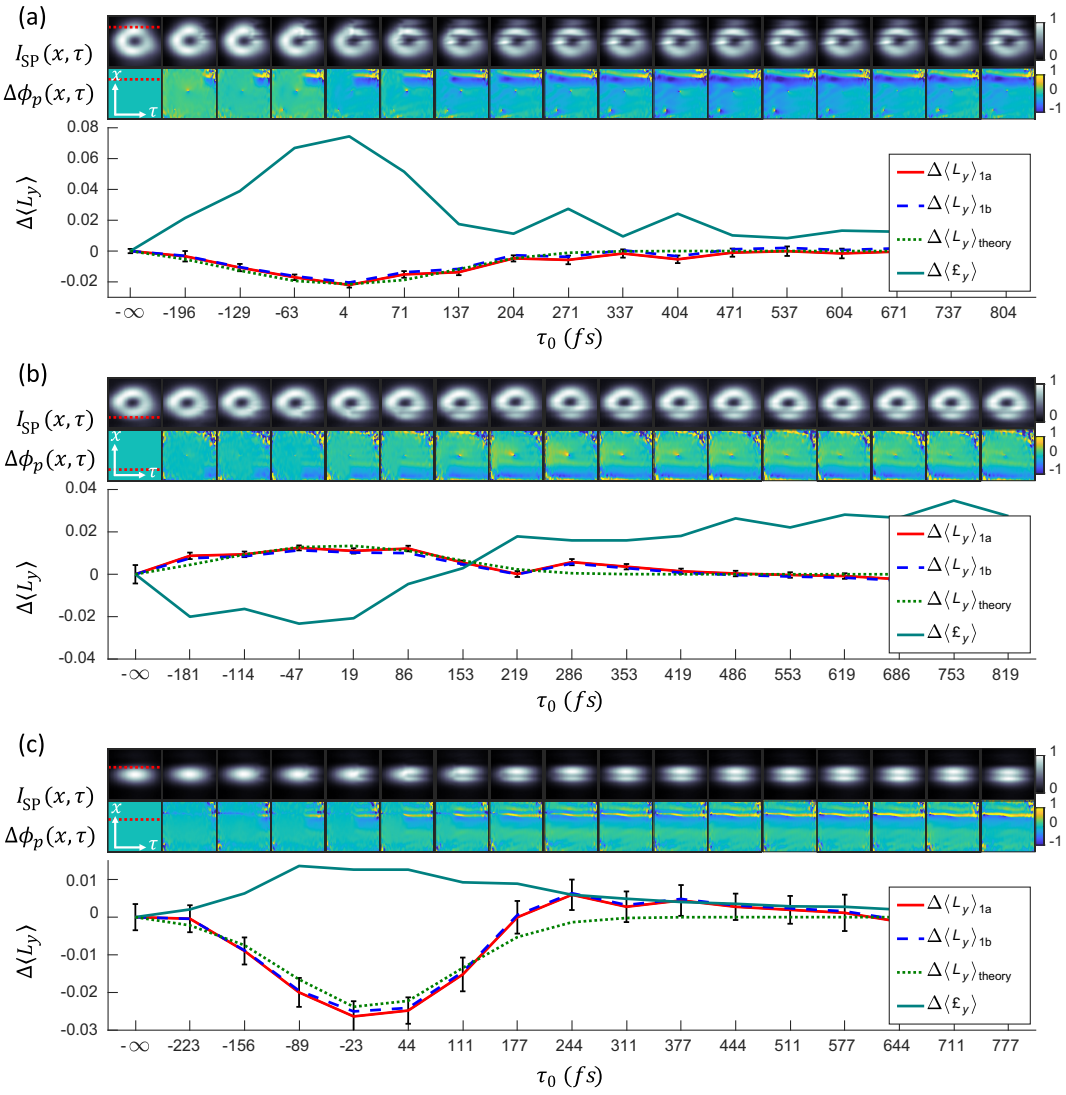

FIG. 9. Comparison of the predictions of Refs. [33,34] against our experimental results. The above panels replot the curves of Fig. 6 and overlay $\Delta\langle \mathcal{L}_y\rangle$, where the latter is computed using Eq. (1a), with the complex fields provided by the TG-SSSI measurements.

$$\langle L_y\rangle_{sp} = u_{sp}^{-1}\int dxd\xi\left[-i|A_s|^2|\Gamma|\left(\xi\frac{\partial|\Gamma|}{\partial x}+\beta_2 x\frac{\partial|\Gamma|}{\partial\xi}\right)-i|\Gamma|^2|A_s|\left(\xi\frac{\partial|A_s|}{\partial x}+\beta_2 x\frac{\partial|A_s|}{\partial\xi}\right)\right.$$
$$\left.+|A_s|^2|\Gamma|^2\left(\xi\frac{\partial\Delta\phi_p}{\partial x}+\beta_2 x\frac{\partial\Delta\phi_p}{\partial\xi}\right)+|A_s|^2|\Gamma|^2\left(\xi\frac{\partial\phi_s}{\partial x}+\beta_2 x\frac{\partial\phi_s}{\partial\xi}\right)\right], \tag{A12b}$$

where the y dependence is integrated out. The first two terms in Eq. (A12b) integrate to zero, yielding

$$\Delta\langle L_y\rangle = \langle L_y\rangle_{sp}-\langle L_y\rangle_s$$
$$= iu_{sp}^{-1}\int dxd\xi\left[|A_s|^2|\Gamma|^2L_y\Delta\phi_p+|A_s|^2\left(|\Gamma|^2-\frac{u_{sp}}{u_s}\right)L_y\phi_s\right]. \tag{A13}$$

For an initial pulse with zero transverse OAM density, such as a Gaussian, $L_y\phi_s = 0$ and

$$\Delta\langle L_y\rangle = iu_{sp}^{-1}\int dxd\xi|A_s|^2|\Gamma|^2L_y\Delta\phi_p. \tag{A14}$$

For a phase-only perturbation $|\Gamma(x,\xi)| = 1$, $u_{sp} = u_s$, and Eq. (A14) also applies.

5. Spatiotemporal torque and STOV formation in femtosecond filamentation

The first experimental measurement of STOVs [11], which were spontaneously generated as a consequence of arrested self-focusing collapse in femtosecond pulse filamentation in air, can be understood in terms of spatiotemporal torque. In air, femtosecond filamentation [43,44] occurs when an ultrashort pulse undergoes self-focusing collapse, which continues and accelerates until the intensity is high enough to ionize air molecules via OFI, with the ultrafast-rise-time plasma then acting to defocus the pulse. The few-femtosecond rise time of the plasma determined by the OFI rate occurs within the pulse temporal envelope. The generated plasma then has a recombination-limited lifetime of several nanoseconds, an extremely long timescale compared to the pulse itself. The phase perturbation imparted by this plasma—responsible for spatiotemporal torque—is therefore quite well modeled by Eq. (4) for $(x_0, \xi_0) = (0, 0)$ and $h/w_{0x} \sim 0.5$, where the filament plasma is centered on the pulse, and its width $2h$ is narrower than the beam width of approximately $2w_{0x}$.

The case of $\beta_2 = 0$ and $h/w_{0x} = 0.5$ [middle right panel in Fig. 2(a)] can apply to filaments, and it gives $\Delta\langle L_y\rangle = 0$ for $(x_0, \xi_0) = (0, 0)$. This is consistent with total transverse OAM of zero in the toroidal STOVs first measured in Ref. [11]. However, the change in transverse OAM density $\Delta M_y(x, \xi) = A^*_{\rm sp} L_y A_{\rm sp}$ [from Eq. (1a)] is nonzero, and this is the effect measured in the experiment of Ref. [11], albeit for a much larger $|\Delta\phi_{p0}|$ accumulated over self-focused propagation in ionizing air. The plots of ΔM_y vs (x, ξ) in Figs. 10(a) and 10(b) show regions of OAM density of opposite sign across the $x = 0$ axis, displaying physics similar to an x-ξ planar slice of the toroidal STOVs of Ref. [11]. Figure 10(a) plots ΔM_y for the simple step-function perturbation of Eq. (4); nonzero ΔM_y regions are only one pixel wide. Figure 10(b) uses Eq. (7), a more realistic perturbation with smoothed step transitions, where we take $(x_0, \xi_0) = (0, 0)$, $h_x/w_{0x} = 0.5$, and $h_\xi/w_{0\xi} = 0.5$.

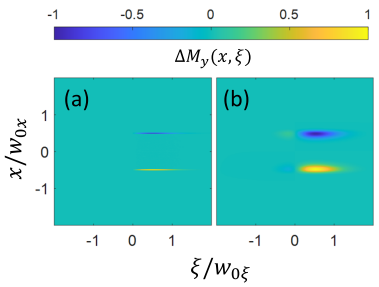

FIG. 10. (a) Change in transverse angular momentum density $\Delta M_y(x, \xi) = A^*_{\rm sp} L_y A_{\rm sp}$ of a Gaussian pulse $A_{\rm G}(x, \xi)$ using step-function perturbation, Eq. (4). (b) Same as (a) except using smoothed perturbation, Eq. (7). In both panels, $\Delta M_y(x, \xi)$ is normalized by the maximum value $|\Delta M_y(x, \xi)|_{\rm max}$.

6. Application of a spatiotemporal phase perturbation localized in space and time

As discussed in Sec. IV, our transient wire spatiotemporal perturbation is well modeled by Eq. (4) or Eq. (7), which describe a narrow spatial structure with a fast turn-on time and no turn-off. To more finely map the effect of spatiotemporal perturbations on electromagnetic pulses, we consider a phase perturbation $\Gamma(x, \xi) = e^{i\Delta\phi_p(x,\xi)}$ localized in both space and time and centered at (x_0, ξ_0): $\Delta\phi_p(x, \xi) = \Delta\phi_{p0} \exp[-(x - x_0)^2/h_x^2 - (\xi - \xi_0)^2/h_\xi^2]$. Figure 11 shows the change in transverse OAM per photon $\Delta\langle L_y\rangle_{x_0,\xi_0}$ for various pulses as a function of (x_0, ξ_0), plotted from analytic expressions determined using Eq. (1a) [45]. In all cases, we take $\beta_2 = 0$ and the perturbation spatial width $h_x/w_{0x} = 0.25$, with the other parameters listed on the panels and in the figure caption.

Examination of Fig. 11(a) for spatiotemporal torque applied to the $l = 1$ STOV pulse of Eq. (5b) confirms our intuitive expectations from Sec. III. Torque is maximized when the perturbation peak (x_0, ξ_0) is placed at the spatiotemporal locations with appreciable energy density and lever arm [see Eq. (3)], while dropping to zero when crossing lines marking the spatial and temporal centers of energy, where torque contributions from opposites sides in space and time cancel. Combined, the two effects give rise to the characteristic four-lobed patterns plotted. A similar pattern appears in the torquing of Gaussian pulses [45]. It is interesting to note that the locations of maximum torque are spatiotemporally outside the peak intensity contour of $A_{\rm STOV}$, which is marked with a dashed red circle. This is the effect of lever arm weighting of the optical energy density in Eq. (3). A weaker four-lobed structure with opposite polarity can be seen inside the peak intensity contour; here, $h_x/w_{0x} = 0.25$ and $h_\xi/w_{0\xi} = 0.25$ are small enough for the perturbation to torque the inside of the STOV "wheel." This structure disappears for the larger values of $h_\xi/w_{0\xi}$ in Fig. 11(b). Also evident is the linear scaling of $\Delta\langle L_y\rangle$ with α, which follows from our theory of STOV transverse OAM [22].

The effect of a temporally widening $\Delta\phi_p(x, \xi)$ of fixed peak amplitude is plotted at the bottom of Fig. 11(b). It is seen that in the middle panel (for the middle pulse width), the torque is both larger in size and is effectively applied over a wider spatiotemporal area than for perturbations of shorter and longer pulse widths. In particular, the very long perturbation of the rightmost panel registers negligible $\Delta\langle L_y\rangle_{x_0,\xi_0}$ anywhere, consistent with the perturbation approaching steady state. The blue curve, just below, plots $|\Delta\langle L_y\rangle_{x_0,\xi_0}|_{\rm max}$, showing that a perturbation transient comparable to the optical pulsewidth ($h_\xi/w_{0\xi} \sim 1$) is most effective in maximizing the duration of torque. For the case of an energy-limited perturbation, increasing its duration h_ξ may result in decreasing $\Delta\phi_{p0}$. The red dashed curve, using the constraint $(h_x h_\xi)^{-1} \int dx d\xi \Delta\phi_p(x, \xi) = 1$, shows this

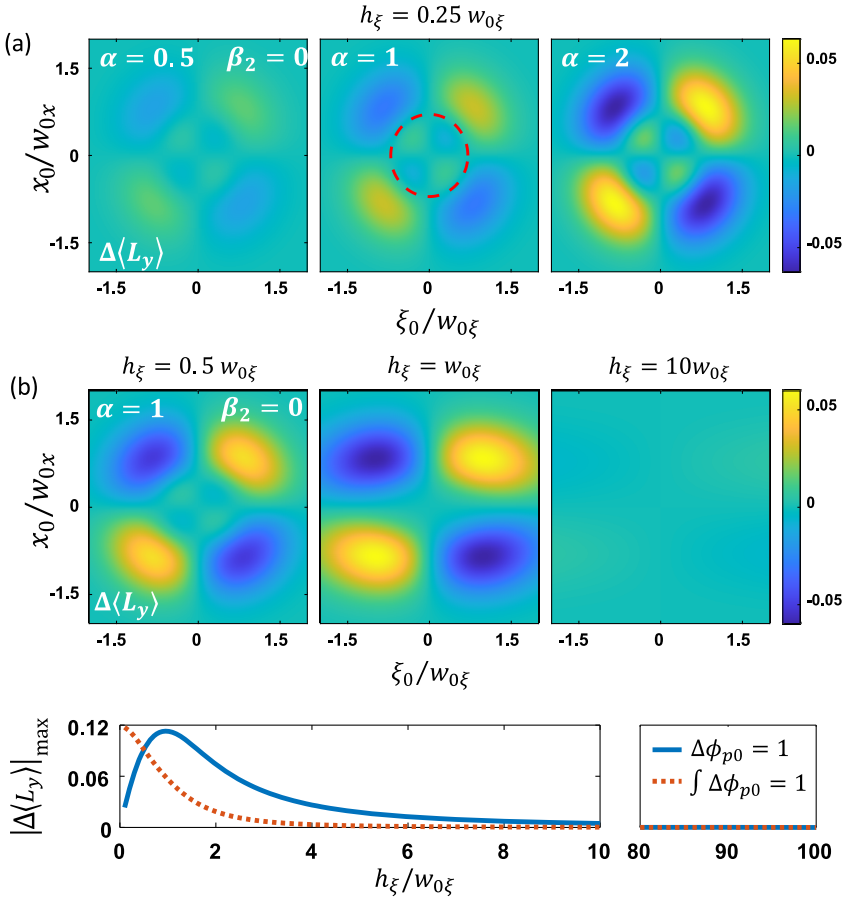

FIG. 11. Plots of analytic solutions [45] for change in transverse OAM per photon, $\Delta\langle L_y\rangle_{x_0,\xi_0}$ imparted to an optical pulse as a function of (x_0, ξ_0) by a spatiotemporal phase perturbation $\Gamma(x,\xi) = \exp[i\Delta\phi_p(x,\xi)]$. Here, $\Delta\phi_p(x,\xi) = \Delta\phi_{p0}\exp[-(x-x_0)^2/h_x^2 - (\xi-\xi_0)^2/h_\xi^2]$, $\Delta\phi_{p0} = 1$, $\beta_2 = 0$, and $h_x/w_{0x} = 0.25$. (a) Perturbation $\Gamma(x,\xi)$ applied to an $l = 1$ STOV pulse $A_{\mathrm{STOV}}(x,\xi) = (\xi/w_{0\xi} + ix/w_{0x})A_{\mathrm{G}}(x,\xi)$ for $h_\xi/w_{0\xi} = 0.25$ and $\alpha = w_{0\xi}/w_{0x} = 0.5$, 1, and 2. The red dashed circle in the center panel is the contour of peak intensity of $|A_{\mathrm{STOV}}|^2$. (b) $\Gamma(x,\xi)$ applied to $A_{\mathrm{STOV}}(x,\xi)$ as in (a), here with $\alpha = 1$ and transient width $h_\xi/w_{0\xi} = 0.5$, 1, and 10. The curves immediately below plot the maximum absolute change in OAM ($|\Delta\langle L_y\rangle_{x_0,\xi_0}|_{\max}$) vs transient width h_ξ, for the cases of fixed peak phase shift $\Delta\phi_{p0} = 1$ and constant integrated phase shift $(h_x h_\xi)^{-1}\int dx d\xi \Delta\phi_p(x,\xi) = 1$. The overlaid dashed red circle follows the maximum intensity contour of A_{STOV}.

effect, where in this case the most effective perturbation is the shortest.

APPENDIX B: PROPAGATION SIMULATIONS

3D + 1 (three space dimensions plus time) simulations of nonparaxial pulse propagation were performed using our unidirectional pulse propagation equation [46,47] implementation called YAPPE [48] for linear propagation in a dispersive medium. YAPPE solves a system of ordinary differential equations,

$$\frac{\partial}{\partial z}\tilde{E}_{k_x,k_y}(\omega,z) = iK_z(\omega,k_x,k_y)\tilde{E}_{k_x,k_y}(\omega,z), \tag{B1a}$$

$$\tilde{E}_{k_x,k_y}(\omega,z) = \tilde{E}_{k_x,k_y}(\omega,z=0)\exp[iK_z(\omega,k_x,k_y)z]. \tag{B1b}$$

Here, $\tilde{E}_{k_x,k_y}(\omega,z) = \mathcal{F}_{x,y,\tau}\{E(x,y,\tau;z)\}$ is the 3D Fourier transform of the spacetime field $E(x,y,\tau;z)$, where $\tau = t - z/v_g(\omega)$, ω is the angular frequency, $v_g(\omega)$ is the frequency-dependent group velocity in the medium, and $K_z(\omega,k_x,k_y) = [(\omega/v_g(\omega))^2 - (k_x^2 + k_y^2)]^{1/2} - \omega/v_g(\omega)$, which models diffraction and dispersion. The transverse wave number (k_x, k_y) indexes the system of equations [Eq. (B1)], which are numerically solved. To recover the field in the spacetime domain, a 3D inverse Fourier transform is performed, $E(x,y,\tau;z) = \mathcal{F}^{-1}_{k_x,k_y,\omega}\{\tilde{E}_{k_x,k_y}(\omega,z)\}$.

APPENDIX C: DETAILED EXPERIMENTAL SETUP

The detailed experimental setup is shown in Fig. 12.

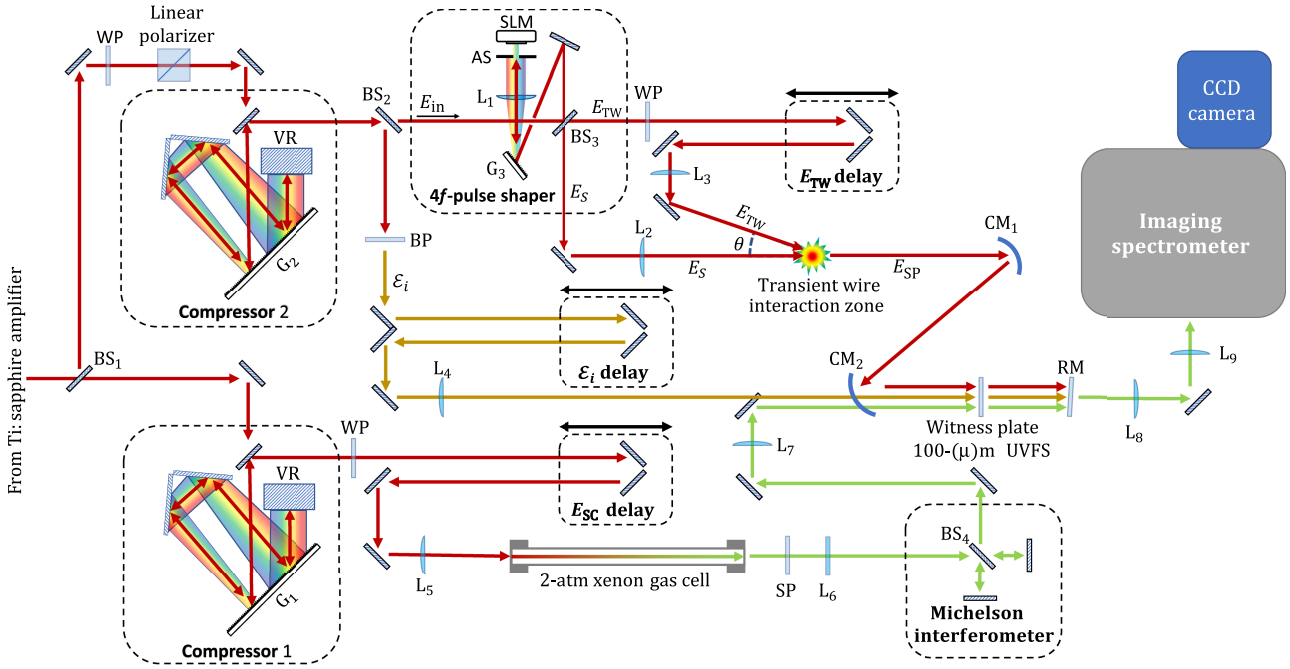

FIG. 12. Detailed experimental configuration. Compressor 1 adjusts the pulse for the $4f$-pulse shaper, TG-SSSI spatial interferometry pulse $\mathcal{E}_i$, and transient wire pulse E_{TW}. Compressor 2 adjusts the pulse for the TG-SSSI probe and reference supercontinuum pulses [17]. CM, concave mirror; BP, bandpass filter 3-nm FWHM, 800-nm center; AS, adjustable slit; SLM, spatial light modulator; WP, $\lambda/2$ wave plate; SP, short-pass filter transmits below 750 nm; VR, vertical retroreflector; RM, pump and interferometric reference rejection mirror; G, grating; L, lens.

[1] L. Allen, M. W. Beijersbergen, R. J. C. Spreeuw, and J. P. Woerdman, *Orbital angular momentum of light and the transformation of Laguerre-Gaussian laser modes*, Phys. Rev. A **45**, 8185 (1992).

[2] Y. Yang, Y. Ren, M. Chen, Y. Arita, and C. Rosales-Guzmán, *Optical trapping with structured light: A review*, Adv. Opt. Photonics **3**, 034001 (2021).

[3] B. M. Heffernan, S. A. Meyer, D. Restrepo, M. E. Siemens, E. A. Gibson, and J. T. Gopinath, *A fiber-coupled stimulated emission depletion microscope for bend-insensitive through fiber imaging*, Sci. Rep. **9**, 11137 (2019).

[4] D. Gauthier, P. Rebernik Ribic, G. Adhikary, A. Camper, C. Chappuis, R. Cucini, L. F. DiMauro, G. Dovillaire, F. Frassetto, R. Geneaux, P. Miotti, L. Poletto, B. Ressel, C. Spezzani, M. Stupar, T. Ruchon, and G. De Ninno, *Tunable orbital angular momentum in high-harmonic generation*, Nat. Commun. **8**, 14971 (2017).

[5] A. Goffin, I. Larkin, A. Tartaro, A. Schweinsberg, A. Valenzuela, E. W. Rosenthal, and H. M. Milchberg, *Optical guiding in 50-meter-scale air waveguides*, Phys. Rev. X **13**, 011006 (2023).

[6] B. Miao, L. Feder, J. E. Shrock, A. Goffin, and H. M. Milchberg, *Optical guiding in meter-scale plasma waveguides*, Phys. Rev. Lett. **125**, 074801 (2020).

[7] C. Paterson, *Atmospheric turbulence, and orbital angular momentum of single photons for optical communication*, Phys. Rev. Lett. **94**, 153901 (2005).

[8] A. E. Willner, K. Pang, H. Song, K. Zou, and H. Zhou, *Orbital angular momentum of light for communications*, Appl. Phys. Rev. **8**, 041312 (2021).

[9] M. Erhard, R. Fickler, M. Krenn, and A. Zeilinger, *Twisted photons: New quantum perspectives in high dimensions*, Light Sci. Appl. **7**, 17146 (2018).

[10] A. Longman and R. Fedosejevs, *Kilo-tesla axial magnetic field generation with high intensity spin and orbital angular momentum beams*, Phys. Rev. Res. **3**, 043180 (2021).

[11] N. Jhajj, I. Larkin, E. W. Rosenthal, S. Zahedpour, J. K. Wahlstrand, and H. M. Milchberg, *Spatiotemporal optical vortices*, Phys. Rev. X **6**, 031037 (2016).

[12] M. Le, G. Hine, and H. M. Milchberg, *Spatiotemporal optical vortices (STOVs) and relativistic optical guiding*, in *Proceedings of the 64th Annual Meeting of the APS Division of Plasma Physics, 2022*, Paper No. NO08.00011, 2022, https://meetings.aps.org/Meeting/DPP22/Session/NO08.11.
[13] K. Y. Bliokh and F. Nori, *Spatiotemporal vortex beams and angular momentum*, Phys. Rev. A **86**, 033824 (2012).
[14] N. Jhajj, *Hydrodynamic and electrodynamic implications of optical femtosecond filamentation*, Ph.D. dissertation, University of Maryland, 2017 [https://drum.lib.umd.edu/handle/1903/19973].
[15] S. Zahedpour, S. W. Hancock, and H. M. Milchberg, *Direct measurement of linearly imposed spatiotemporal optical vortices (STOVs)*, in *Frontiers in Optics+Laser Science APS/DLS, OSA Technical Digest* (Optica Publishing Group, Washington, DC, 2019), 10.1364/FIO.2019.FW5F.5.
[16] S. W. Hancock, S. Zahedpour, A. Goffin, and H. M. Milchberg, *Free-space propagation of spatiotemporal optical vortices*, Optica **6**, 1547 (2019).
[17] S. W. Hancock, S. Zahedpour, and H. M. Milchberg, *Transient-grating single-shot supercontinuum spectral interferometry (TG-SSSI)*, Opt. Lett. **46**, 1013 (2021).
[18] A. Chong, C. Wan, J. Chen, and Q. Zhan, *Generation of spatiotemporal optical vortices with controllable transverse orbital angular momentum*, Nat. Photonics **14**, 350 (2020).
[19] S. Zahedpour, S. W. Hancock, and H. M. Milchberg, *Orbital angular momentum conservation in second-harmonic generation with spatiotemporal optical vortices*, in *Frontiers in Optics+Laser Science APS/DLS, OSA Technical Digest* (Optical Society of America, Washington, DC, 2020), 10.1364/FIO.2021.JTh5A.29.
[20] S. W. Hancock, S. Zahedpour, and H. M. Milchberg, *Second-harmonic generation of spatiotemporal optical vortices*, in *High-Brightness Sources and Light-Driven Interactions Congress, OSA Technical Digest* (Optical Society of America, Washington, DC, 2020), 10.1364/EUVXRAY.2020.JM3A.21.
[21] S. W. Hancock, S. Zahedpour, and H. M. Milchberg, *Second-harmonic generation of spatiotemporal optical vortices and conservation of orbital angular momentum*, Optica **8**, 594 (2021).
[22] S. W. Hancock, S. Zahedpour, and H. M. Milchberg, *Mode structure and orbital angular momentum of spatiotemporal optical vortex pulses*, Phys. Rev. Lett. **127**, 193901 (2021).
[23] H. Wang, C. Guo, W. Jin, A. Y. Song, and S. Fan, *Engineering arbitrarily oriented spatiotemporal optical vortices using transmission nodal lines*, Optica **8**, 966 (2021).
[24] J. Huang, J. Zhang, T. Zhu, and Z. Ruan, *Spatiotemporal differentiators generating optical vortices with transverse orbital angular momentum and detecting sharp change of pulse envelope*, Laser Photonics Rev. **16**, 2100357 (2022).
[25] L. L. Doskolovich, A. I. Kashapov, E. A. Bezus, and D. A. Bykov, *Spatiotemporal optical differentiation and vortex generation with metal-dielectric-metal multilayers*, Phys. Rev. A **106**, 033523 (2022).
[26] V. B. Novikov and T. V. Murzina, *Nonlocality-mediated spatiotemporal optical vortex generation in nanorod-based epsilon-near-zero metamaterials*, Opt. Lett. **48**, 2134 (2023).
[27] Y. Fang, S. Lu, and Y. Liu, *Controlling photon transverse orbital angular momentum in high harmonic generation*, Phys. Rev. Lett. **127**, 273901 (2021).
[28] Y. Wu, Z. Nie, F. Li, C. Zhang, K. A Marsh, W. B. Mori, and C. Joshi, *Spatial and spatiotemporal vortex harmonics carrying controllable orbital angular momentum generated by plasma mirrors*, in *Proceedings of the Optica Nonlinear Optics Topical Meeting* (Optica Publishing Group, Washington, DC, 2023), 10.1364/NLO.2023.M2B.6.
[29] H. Ge, S. Liu, X. Y. Xu, Z. W. Long, Y. Tian, X. P. Liu, M. H. Lu, and Y. F. Chen, *Spatiotemporal acoustic vortex beams with transverse orbital angular momentum*, Phys. Rev. Lett. **131**, 014001 (2023).
[30] H. Zhang, Y. Sun, J. Huang, B. Wu, Z. Yang, K. Y. Bliokh, and Z. Ruan, *Topologically crafted spatiotemporal vortices in acoustics*, Nat. Commun. **14**, 6238 (2023).
[31] A. Aiello, N. Lindlein, C. Marquardt, and G. Leuchs, *Transverse angular momentum and geometric spin Hall effect of light*, Phys. Rev. Lett. **103**, 100401 (2009).
[32] A. Aiello, C. Marquardt, and G. Leuchs, *Transverse angular momentum of photons*, Phys. Rev. A **81**, 053838 (2010).
[33] K. Y. Bliokh, *Spatiotemporal vortex pulses: Angular momenta and spin-orbit interaction*, Phys. Rev. Lett. **126**, 243601 (2021).
[34] K. Y. Bliokh, *Orbital angular momentum of optical, acoustic, and quantum-mechanical spatiotemporal vortex pulses*, Phys. Rev. A **107**, L031501 (2023).
[35] H. He, M. E. J. Friese, N. R. Heckenberg, and H. Rubinsztein-Dunlop, *Direct observation of transfer of angular momentum to absorptive particles from a laser beam with a phase singularity*, Phys. Rev. Lett. **75**, 826 (1995).
[36] H. F. Elder and P. Sprangle, *Mode power spectrum for Laguerre-Gauss beams in Kolmogorov turbulence*, Opt. Lett. **47**, 3447 (2022).
[37] J. D. Jackson, *Classical Electrodynamics*, 2nd ed. (Wiley, New York, 1975), p. 604.
[38] M. Panahi, R. Shomali, M. Mollabashi, and S. Rasouli, *Atmospheric coherence time measurement by 4-aperture DIMM defocus velocity technique*, Appl. Opt. **58**, 8673 (2019).
[39] M. A. Porras, *Transverse orbital angular momentum of spatiotemporal optical vortices*, Prog. Electromagn. Res. **177**, 95 (2023).
[40] M. V. Berry, *Paraxial beams of spinning light*, Proc. SPIE Int. Soc. Opt. Eng. **3487**, 6 (1998).
[41] I. Bialynicki-Birula, *Photon wave function*, Prog. Opt. **36**, 245 (1996).
[42] A. S. Desyatnikov, D. Buccoliero, M. R. Dennis, and Y. S. Kivshar, *Spontaneous knotting of self-trapped waves*, Sci. Rep. **2**, 771 (2012).
[43] A. Couairon and A. Mysyrowicz, *Femtosecond filamentation in transparent media*, Phys. Rep. **441**, 47 (2007).
[44] L. Bergé, S. Skupin, R. Nuter, J. Kasparian, and J.-P. Wolf, *Ultrashort filaments of light in weakly ionized, optically transparent media*, Rep. Prog. Phys. **70**, 1633 (2007).

[45] See Supplemental Material at http://link.aps.org/supplemental/10.1103/PhysRevX.14.011031 calculations on spatiotemporal phase and amplitude perturbations localized in time and space.

[46] M. Kolesik and J. V. Moloney, *Nonlinear optical pulse propagation simulation: From Maxwell's to unidirectional equations*, Phys. Rev. E **70**, 036604 (2004).

[47] A. Couairon, E. Brambilla, T. Corti, D. Majus, O. Ramirez-Gongora, and M. Kolesik, *Practitioner's guide to laser pulse propagation models and simulation*, Eur. Phys. J. Special Topics **199**, 5 (2011).

[48] L. Feder, B. Miao, J. E. Shrock, A. Goffin, and H. M. Milchberg, *Self-waveguiding of relativistic laser pulses in neutral gas channels*, Phys. Rev. Res. **2**, 043173 (2020).